

Giant Diffusion in a two-dimensional Neuron Model

MASTERARBEIT

zur Erlangung des akademischen Grades
Master of Science
(M. Sc.)
im Fach Physik



eingereicht an der
Mathematisch-Naturwissenschaftlichen Fakultät I
Institut für Physik
Humboldt-Universität zu Berlin

von
Richard Kullmann
geboren am 17.07.1996 in Berlin-Pankow

Gutachter:

1. *Prof. Dr. Oliver Benson*
2. *Prof. Dr. Kurt Busch*

eingereicht am: *8. Februar 2018*

Abstract

The emerging field of magnetometry based on NV centers opens a variety of new experimental perspectives, including the imaging of single nuclear spins on the nanoscale. However, in order to achieve exceptionally long NV electron spin coherence times and high sensitivities, the NV spin needs to be decoupled from unwanted interactions with the environment. This can be accomplished with dynamical decoupling sequences.

During the work for this thesis, multiple dynamical decoupling protocols were implemented and tested on NV centers in bulk diamond and nanodiamond. The theoretical part covers general NV properties before treating the behaviour of a free electron spin and finally applying this on the NV center. Then, the effect of different decoupling protocols are discussed. After that, the structure and concept of the setup will be explained. In the final part, the measurements will be presented. The execution of the decoupling sequences will be demonstrated and the data will be used to extract the spectral density function of the environment.

It was shown that all implemented dynamical decoupling sequences could enhance the coherence time. It was demonstrated that CPMG outperforms the other sequences on the given setup, achieving an improvement of up to a factor of 200 in the bulk diamond and 50 in nanodiamond. Finally, the examination of the spectral density functions of the spin bath gave a deeper insight in its coupling strength to the NV and its internal dynamics.

In the future, the limitations of the sequences will be further explored and other decoupling protocols will be tested. In addition to that, a better time and phase control has to be accomplished. These efforts will eventually lead to sensitivities high enough to detect small spin ensembles and even single molecular spins.

Contents

1	Introduction	1
2	Models and Methods	6
2.1	The $I_{Na,p} + I_K$ model with saddle-node bifurcation	6
2.1.1	System without noise	6
2.1.2	System with noise	10
2.1.3	System with periodic signal	11
2.2	$I_{Na,p} + I_K$ model with subcritical Andronov-Hopf bifurcation	11
2.2.1	System without noise	12
2.2.2	System with noise	15
2.3	Rinzel model	16
2.3.1	System without noise	17
2.3.2	System with noise	20
2.4	Quantities of interest	21
2.4.1	System without signal	21
2.4.2	System with signal	22
2.5	Two-state theory	23
2.5.1	Fano factor in weak noise limit	23
2.5.2	Behavior of SNR	24
2.6	Numerical implementation	24
2.6.1	Simulation parameters	24
2.6.2	Numerical subtleties	25
3	Critical currents in the Fano factor	26
3.1	Count statistics	26
3.1.1	$I_{Na,p} + I_K$ -model with saddle-node bifurcation	26
3.1.2	$I_{Na,p} + I_K$ model with subcritical Andronov-Hopf bifurcation	29
3.1.3	Rinzel model	32
3.1.4	Influence of the initial conditions	35
3.1.5	Conclusion	36
4	Transition rates in bistable neurons	36
4.1	$I_{Na,p} + I_K$ model with saddle node bifurcation	36
4.1.1	Distribution of the state lifetimes	36
4.1.2	Transition rates at different noise intensities	37
4.1.3	Arrhenius Plots and effective potential barriers	38
4.1.4	Comparison with two-state theory	40
4.2	$I_{Na,p} + I_K$ model with Andronov-Hopf bifurcation	42
4.2.1	Distribution of the state lifetimes	42
4.2.2	Transition rates at different noise intensities	43
4.2.3	Arrhenius Plots and effective potential barriers	43
4.3	Rinzel model with saddle-node bifurcation	45
4.3.1	Transition rates at different noise intensities	46
4.3.2	Arrhenius Plots and effective potential barriers	46

5	Consequences for Signal transmission	48
5.1	$I_{Na,p} + I_K$ model with saddle-node bifurcation	49
5.2	$I_{Na,p} + I_K$ model with Andronov-Hopf bifurcation	52
5.3	Rinzel model with saddle-node bifurcation	55
6	Conclusions	56

1 Introduction

The human brain is one of the most investigated but still least understood subjects in scientific research. This comes as no surprise considering the huge variety of tasks it can perform efficiently and seemingly effortlessly: it constantly combines multiple sensory impressions and filters the most relevant of them to form a coherent image of the surroundings, it remembers information it has learned decades ago, it can produce the most complex thoughts and keep a whole organism working properly in the meantime. And despite the mayor improvement of processor performance and increasing interest in machine learning and artificial neural networks during the past couple of years, no technological implementation has even remotely managed to match the capability of the human brain.

The basis for its high functionality lies in the huge number of neurons - around 100 Billions[1] - and their interconnectivity: neural cells usually receive inputs from more than 10.000 other neurons[2]. Thus, in order to be able to understand how the brain works and possibly derive future applications from that, it is crucial to examine neural cells and study their characteristics.

Neural cells display a plethora of responses to their synaptic inputs. In general, neural activity can be divided into four mayor regimes: resting state, sub-threshold oscillations, spiking and bursting[3]. Often, multiple of these regimes can be found in a single neuron. Of particular interest is the bistability between resting and spiking activity. This has been observed in pacemaker[4], sensory [5][6] and motoneurons[7][8] and is suggested to play important roles in short term memory and processing[6][9][10] as well as in shaping patterns of spindling oscillations[11].

As each regime displays different voltage dynamics, a bistability in neural activity directly translates into a bistability of the membrane voltage. When noise is added to the system, stochastic switchings between the states will occur. That way, the bistable system is turned into a stochastically bursting neuron model. If the noise intensity is small in comparison to the other ionic currents, the membrane voltage takes on a rectangular shape. In the resting state, the voltage performs noise-driven oscillations around the stable equilibrium point and in the firing state, it may perform large oscillations around the same stable equilibrium or rotate around an unstable focus. This is illustrated in figure 1.

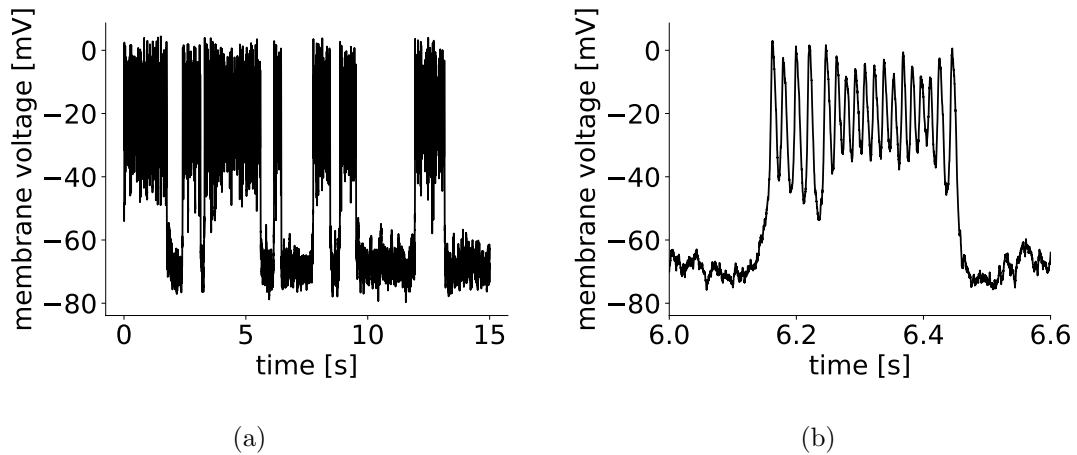


Figure 1: Example of bistable membrane voltage under the influence of noise. The amplification in (b) illustrates the different qualitative behaviors in both regimes.

A similar bistability has been observed for Brownian Particles in a tilted periodic potential, obeying the following equations of motion[12]:

$$\dot{v} = -\gamma v - U'(x) + \sqrt{2\gamma kT}\xi(t) \quad (1)$$

with the potential $U(x) = -Fx - d\cos(x)$. γ is the friction coefficient, kT the thermal energy which corresponds to the noise intensity and the bias force F determines the tilt of the potential.

Assuming that friction is low and F is chosen such that the tilted potential keeps its minima and maxima, the Brownian particle can be in two different velocity states (figure 2). If it performs noise-induced oscillations near a minimum, it is in the so-called *locked state*. After the Brownian particle has managed to overcome a hill and still has enough energy to pass the adjacent maxima as well, it is said to be in the *running state*. While making its way down the washboard potential, the Brownian particle constantly switches between these states due to the influence of noise.

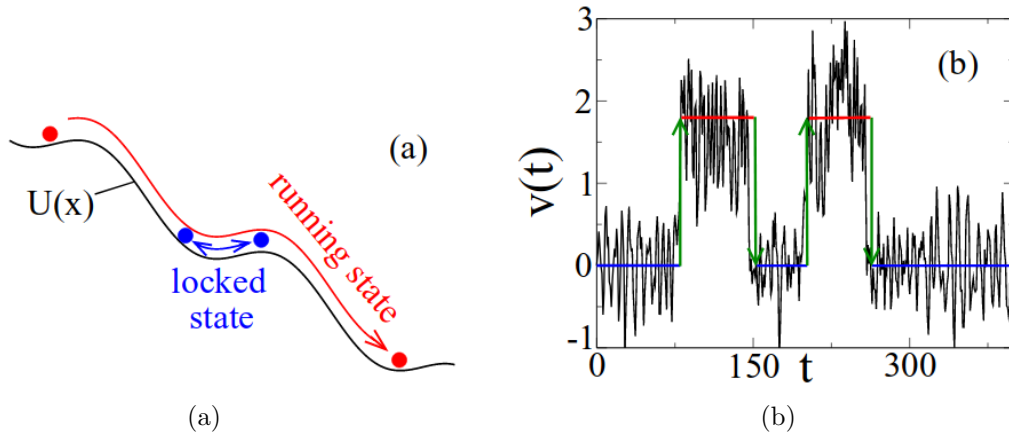


Figure 2: Figure (a) visualizes the two motional states of a Brownian Particle in a periodic potential, on the right one can see the bistable velocity dynamics. The oscillations in the locked state are noise-induced while they mainly arise from local extrema of the potential in the running state. These images have been taken from[12].

In the case of large friction or a strongly tilted potential, however, the particle will barely move or move almost all of the time, respectively. In either configuration, one of the states prevails. When a couple of Brownian Particles are thrown into the system under these conditions, the majority of particles finds itself in the same state of motion. As a consequence, the particles move roughly as a group with only little spread around the mean velocity. Therefore, the effective diffusion coefficient D_{eff} which quantifies the diffusional spread,

$$D_{eff} = \lim_{t \rightarrow \infty} \frac{\langle x^2(t) \rangle - \langle x(t) \rangle^2}{2t} \quad (2)$$

becomes very small. The other extreme case is reached when the parameters are chosen in such a way that both states are equally likely. Then, approximately half of the particles are resting while the others are in the running state, leading to a large D_{eff} . The lower the noise intensity, the fewer switchings occur and the higher is the effective diffusion coefficient. This phenomenon can be seen in figure (3).

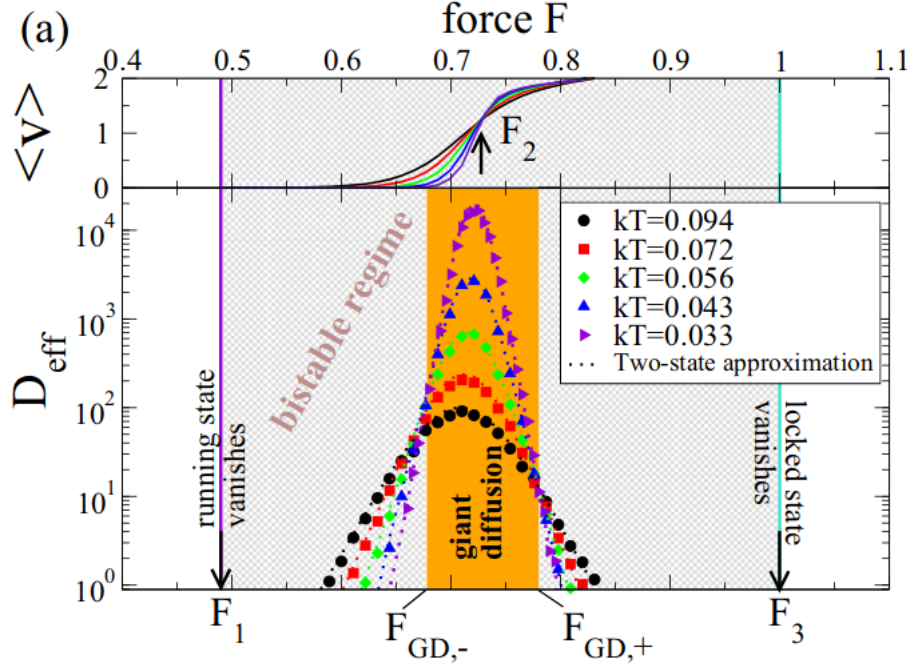


Figure 3: Simulation of velocity and effective diffusion coefficient for Brownian Particles in a tilted periodic potential, taken from [12]

The upper part of the picture shows the average velocity which naturally increases with the slope of the potential. Depending on the friction, there is a bias force - here denoted by F_2 - where frictional loss and acceleration via the potential annihilate each other. In the zero-noise limit, bias forces which are smaller than this value lead to a vanishing velocity, as the running state cannot be sustained without noise. The same argument can be made for $F > F_2$: as the running state cannot be stopped without noise, the maximum velocity is achieved. Consequently, all velocity curves make a jump and intersect each other at F_2 .

As explained above, the diffusion coefficient gets maximal when both states are occupied with equal probabilities, which obviously happens at F_2 . Interestingly, the Giant Diffusion is not only restricted to this particular bias force, but extends over a finite area between the two intersection points of all curves, $F_{GD,\pm}$. Outside of this region, D_{eff} decreases with the noise intensity. Taking a closer look, one notices that the left intersection lies slightly above the right one.

It should be noted that a motion with low diffusion as it occurs outside the region of Giant Diffusion does not require the disappearance of one of the states, but happens much earlier. Thus, not all particles need to be in the same motional state to accomplish a small diffusion.

In order to better understand what happens in the bistable regime, a simplified description can be used. In the case of low noise intensity, the transition times between the locked state and the running state will be much shorter than the periods of time that the particle stays in one of the two states. That is why it is practical to describe the behavior of the system with a two-state model. The results of this model are plotted as dotted curves and show good agreement with the data. The

transition rates between the states are assumed to obey an Arrhenius law:

$$r_{\pm} = r_{0,\pm} \exp\left(-\frac{\Delta U_{\pm}}{D}\right) \quad (3)$$

where r_- denotes the transition rate from locked to running state, and r_+ the rate for the other transition. ΔU_{\pm} is the corresponding potential barrier that needs to be traversed and D the noise intensity which previously was kT . The effective diffusion coefficient can be calculated from the velocity v_0 in the running state and the transition rates[13]:

$$D_{\text{eff}} = \frac{v_0^2 r_+ r_-}{(r_+ + r_-)^3} \quad (4)$$

This formula allows us to find the intersection points of the diffusion coefficients. As the curves for all noise intensities go through these points, they become independent of the noise intensity there. It is

$$\begin{aligned} D_{\text{eff}} &= \frac{v_0^2 r_{0,+} r_{0,-} \exp\left(-\frac{\Delta U_+ + \Delta U_-}{D}\right)}{\left[r_{0,+} \exp\left(-\frac{\Delta U_+}{D}\right) + r_{0,-} \exp\left(-\frac{\Delta U_-}{D}\right)\right]^3} \\ &= \frac{v_0^2 r_{0,+} r_{0,-}}{\left[r_{0,+} \exp\left(-\frac{3\Delta U_+ - \Delta U_+ - \Delta U_-}{3D}\right) + r_{0,-} \exp\left(-\frac{3\Delta U_- - \Delta U_+ - \Delta U_-}{3D}\right)\right]^3} \\ &= \frac{v_0^2 r_{0,+} r_{0,-}}{\left[r_{0,+} \exp\left(-\frac{2\Delta U_+ - \Delta U_-}{3D}\right) + r_{0,-} \exp\left(-\frac{2\Delta U_- - \Delta U_+}{3D}\right)\right]^3} \end{aligned}$$

In the limes $D \rightarrow 0$, $\Delta U_+ > U_-$ the first term in the denominator vanishes, resulting in:

$$D_{\text{eff}} = \frac{v_0^2 r_{0,+}}{r_{0,-}^2} \exp\left(-\frac{\Delta U_+ - 2\Delta U_-}{D}\right)$$

Under the assumption that the prefactors change slowly in comparison to the exponential function, the following condition arises:

$$\Delta U_+ = 2\Delta U_- \quad (5)$$

Due to symmetry of the problem, the opposing case $D \rightarrow 0$, $\Delta U_+ < U_-$ yields:

$$\Delta U_- = 2\Delta U_+$$

In both cases, one potential barrier is twice as high as the other one.

The verification of this criterion requires knowledge of potential barriers. As there are no actual potential barriers in the system, it is only possible to derive effective barriers from the behavior of the system. These can be acquired by measuring transition rates at different noise intensities and fitting them with the Arrhenius law from (3), as it was done in Figure 4.

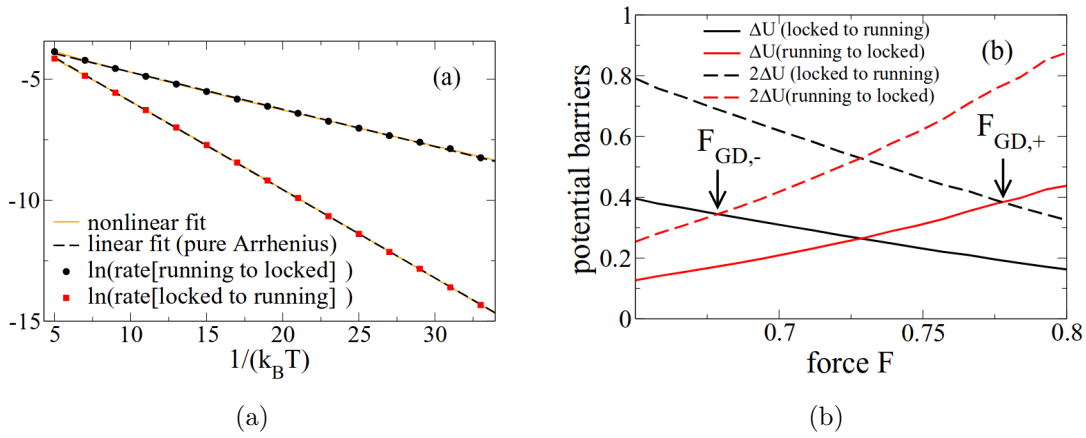


Figure 4: The left shows the transition rates for a fixed bias force over a range of different noise intensities. Fits were done with both an Arrhenius and a Kramers law but yielded similar results for the effective barriers. On the right one can see the effective potential barriers, where the dotted curves are simply twice the solid curves. The images have been taken from [12].

It can be seen that the Arrhenius-like behavior continues over a wide range of noise intensities, allowing to get reliable values for the effective potential barriers. According to the criterion from (5), the critical forces are expected to be at 0.68 and 0.76, which roughly corresponds to the actual intersection points. Consequently, the bistable system at hand could be well described by the two-state theory. This implies that other resembling systems might show similar behavior, as for example bistable neurons. The quantities corresponding to position and velocity would be spike count and firing rate, and the noise source wouldn't be the temperature anymore, but channel noise or random input from surrounding neurons. Instead of a critical bias force, there would be a critical bias current which needed to be crossed to reach Giant Diffusion. One of the most important aspects of this similarity would be signal transmission. If the system is driven by a slow cosine signal with amplitude ϵ , the signal-to-noise ratio can be computed via[14]

$$SNR = \frac{\epsilon^2 T |\chi(0)|^2}{8 D_{eff}}$$

where T denotes the total simulation time. Near the critical current, the spike count diffusion would change by multiple orders of magnitude, leading to a similar change in the SNR.

All in all, bistable neuron models are suggested to exhibit Giant Diffusion and therefore possess critical currents. When the system is near such a critical point, slight changes in the bias current can cause great changes in the SNR and possibly a large enhancement of signal transmission. The goal of this thesis is to find out whether Giant Diffusion exists for neuron models, to identify the critical currents and to investigate the system under the influence of slow periodic signals.

2 Models and Methods

2.1 The $I_{Na,p} + I_K$ model with saddle-node bifurcation

The main focus of this thesis lies on the study of the $I_{Na,p} + I_K$ -model, the persistent sodium plus potassium model with additive noise:

$$C\dot{V} = I - g_L(V - E_L) - g_{Na}m_\infty(V)(V - E_{Na}) - g_Kn(V - E_K) + \sqrt{2D}\xi(t) \quad (6)$$

$$\dot{n} = (n_\infty(V) - n)/\tau(V) \quad (7)$$

Here, V denotes the membrane voltage, C is the capacitance, I is the bias current, g_i are conductances and E_i the Nernst equilibrium potentials. The overall noise intensity is D . Lastly, m_∞ is the activation variable of the instantaneous Na^+ current, while n governs the variation of the slower K^+ current. The steady-state activation functions are approximated by the Boltzmann-function:

$$f_\infty(V) = \frac{1}{1 + \exp\{(V_{1/2} - V)/k\}}$$

At $V_{1/2}$, the activation function has the value $1/2$, and k is the slope factor determining the steepness around $V_{1/2}$ - a smaller value of k leads to a more abrupt change of f_∞ . This approximation was suggested by Izhikevich [2].

The fastest neural oscillations in the human brain are gamma waves with frequencies in the range between 25 and 100 Hz[15][16]. Similar values can also be found in different papers about bursting neurons[17][18]. Therefore, the parameters were chosen such that the frequency in the bursting state was about 70 Hz. The exact values used in the simulations were:

$$C = 1, g_L = 0.3, E_L = -80, g_{Na} = 1, E_{Na} = 60, g_K = 0.4, E_K = -90.$$

Instantaneous Na^+ current:

$$k_m = 14, V_{1/2,m} = -18.$$

K^+ current:

$$k_n = 5, V_{1/2,n} = -25, \tau(V) = \text{const} = 3.$$

2.1.1 System without noise

The qualitative behavior of the neural model can be best understood by first considering the noiseless system. For a system that depends on the evolution of two state variables, in this case V and n , some qualitative and quantitative analysis can be carried out in the phase plane. A neat way to obtain information about an unknown system is to calculate its nullclines. The nullclines are curves in the phase plane, where one of the state variables remains constant. Thus, the V -nullcline is defined by the condition $\dot{V} = 0$ and the n -nullcline follows from $\dot{n} = 0$. By crossing one of the nullclines, the system changes its direction of motion with respect to the corresponding variable. As a consequence, each nullcline separates the phase space into two regions where one of the variables evolves in opposite directions. Taken

together, the nullclines define four different regions of directions: one region each where both variables decrease or increase and two regions where one variable increases and the other decreases. Depending on the specific shape of the nullclines, these regions do not necessarily have to be coherent.

The V -nullcline can be obtained by setting the left side of equation (6) to zero. In the V - n -plane, it can then be described by the function

$$n(V) = \frac{I - g_L(V - E_L) - g_{Na}m_\infty(V)(V - E_{Na})}{g_K(V - E_K)} \quad (8)$$

The n -nullcline is just

$$n(V) = n_\infty(V) \quad (9)$$

The nullclines of the $I_{Na,p} + I_K$ -model are shown in figure 5.

A second aspect of the nullclines are their intersection points. As both state variables remain constant when the nullclines intersect, these points are equilibrium points. In general, there are three different types of equilibria: nodes, saddles and foci. These may be stable or unstable. Any trajectory in the phase space starting close enough to a stable equilibrium stays near it for all times. In contrast to that, an equilibrium is unstable, if at least one trajectory that starts arbitrarily close to it diverges from the equilibrium. If they are in the vicinity of a node, all trajectories either converge to or diverge from it. In the case of a saddle, most trajectories first approach the equilibrium point and then diverge from it. Trajectories that start near a focus rotate around the equilibrium point and thereby get closer to or farther away from it. The equilibrium points can be characterized by studying the Jacobian matrix of the system at these points. A two-dimensional system can be written in the form

$$\dot{x} = f(x, y) \quad (10)$$

$$\dot{y} = g(x, y) \quad (11)$$

Utilizing the fact that the functions f and g can be linearized near the equilibrium, which means they can be approximated by the first term of their Taylor expansion, one finds a linear system at the equilibrium (x_0, y_0) :

$$\begin{pmatrix} \dot{u} \\ \dot{w} \end{pmatrix} = \begin{pmatrix} a & b \\ c & d \end{pmatrix} \begin{pmatrix} u \\ w \end{pmatrix} = L \begin{pmatrix} u \\ w \end{pmatrix} \quad (12)$$

where $u = x - x_0$, $w = y - y_0$, L is the Jacobian matrix at equilibrium and the coefficients are the partial derivatives

$$a = \frac{\partial f}{\partial x}(x_0, y_0), \quad b = \frac{\partial f}{\partial y}(x_0, y_0) \quad (13)$$

$$c = \frac{\partial g}{\partial x}(x_0, y_0), \quad d = \frac{\partial g}{\partial y}(x_0, y_0) \quad (14)$$

Having determined the eigenvalues λ_\pm and eigenvectors \mathbf{v}_\pm of L , a solution for the linear system can be constructed:

$$\begin{pmatrix} u(t) \\ w(t) \end{pmatrix} = c_+ \mathbf{v}_+ \exp(\lambda_+ t) + c_- \mathbf{v}_- \exp(\lambda_- t) \quad (15)$$

At this point, the connection between the Jacobian matrix and the different types of equilibria becomes clear. If both eigenvalues are real and have the same sign, both terms of the solution either grow or decay exponentially, meaning that the equilibrium is a node. If they are real with opposite signs, the equilibrium point is a saddle. Finally, if the eigenvalues are complex-conjugate, the solution oscillates, which makes the equilibrium a focus[2].

When no bias current is applied (that is, $I=0$), the system features three equilibrium points:

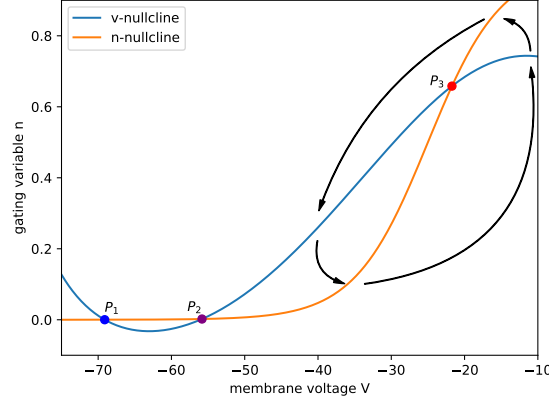


Figure 5: Nullclines of the $I_{Na,p} + I_K$ -model with $I = 0$. The arrows indicate the direction of motion in the different regions.

Carrying out the phase plane analysis, one finds:

$$\begin{array}{ll} \lambda_+(P_1) \approx -0.1 & \lambda_-(P_1) \approx -0.3 \\ \lambda_+(P_2) \approx 0.1 & \lambda_-(P_2) \approx -0.3 \\ \lambda_+(P_3) \approx 0.05 + 0.5i & \lambda_-(P_3) \approx 0.05 - 0.5i \end{array}$$

This means that P_1 is a stable node, P_2 is a saddle point and P_3 is an unstable focus. Thus, in the bursting state, the phase vector will rotate around P_3 , approach P_2 in n - direction and then go away from P_2 in V - direction in order to do another rotation around P_3 .

However, this applies only to the case of small bias currents. When $I \approx 0.36$, the saddle and the node fall together and the system undergoes a saddle-node bifurcation off invariant circle. In this case, the resting state vanishes and the neuron is in a state of tonic spiking.

Provided that we are in the bistable regime, a system with arbitrary initial conditions will either go to the resting or the running state and will not change its behavior anymore after a short period of equilibration, as can be seen in figure 6.

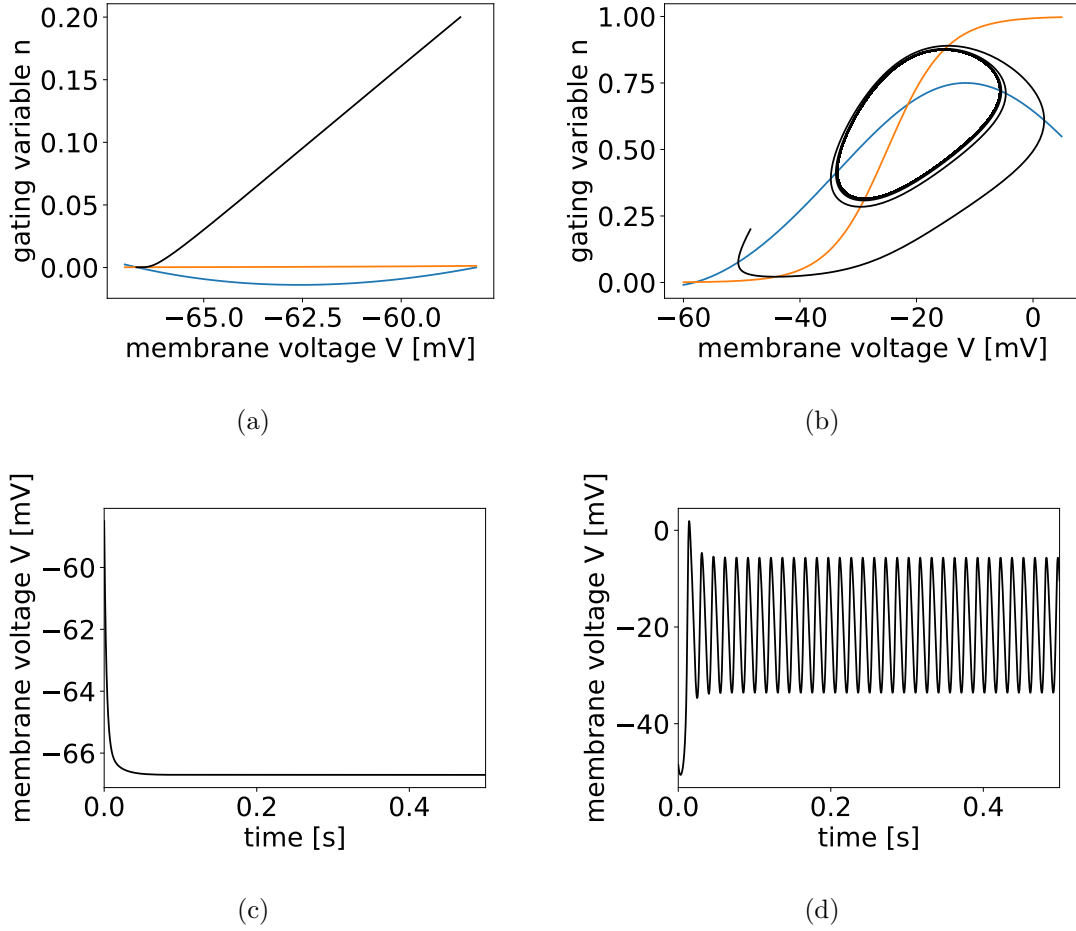


Figure 6: Evolution of the phase vector (first row) and the membrane voltage over time (second row). The left side shows the evolution of the system with resting ICs, and on the right one can see the behavior under spiking ICs.

Analytically, it is hardly possible to determine whether a specific starting point (V_0, n_0) leads to repetitive spiking or no spiking at all. The only thing one can say for sure is that the line that separates both domains will go through the saddle point that was found in the phase plane analysis. Assuming that the gating variable does not change, any trajectory starting at higher voltages will lead to spiking while all trajectories at lower voltage converge to the stable node. A numerical investigation of the model without noise confirms our presumptions (figure 7).

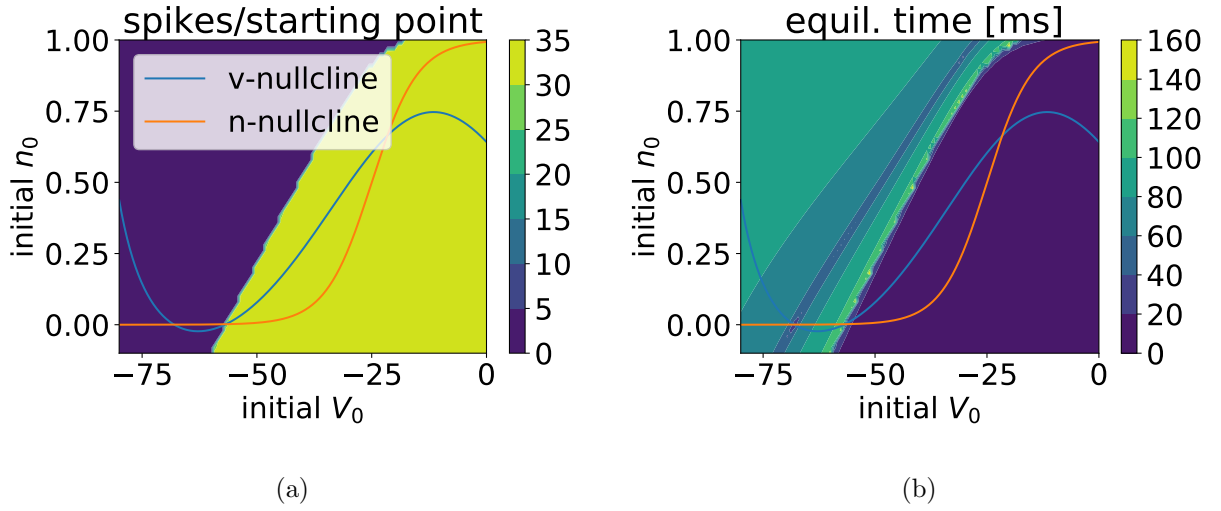


Figure 7: Phase plane image of the neuron model with $I = 0.1$ and no noise. Each point represents a specific combination of starting parameters. The left plot shows the number of spikes over a short period of time and for the right picture, the equilibration times for both states were measured. Irregularities arise from the finite resolution of the V_0 - n_0 -lattice.

There are two distinct regions which can be separated by a monotonically increasing curve that passes through the saddle point. In figure 7b one can see a small intermediate area of large equilibration times. If the system parameters lie in the vicinity of this transition area, a small perturbation suffices to bring the system into either state. Remarkably, most of this area is made up by starting points leading to the stable equilibrium while only a small streak consists of bursting initial conditions. Consequently, the running state is reached much faster than the resting state.

2.1.2 System with noise

When noise is brought into the system, the findings for the noiseless system still apply to a great extent. Starting in one of the two domains, the system will most likely first converge to the corresponding state, and the time it takes for that will be about the same as before. However, the system will not stay in this state forever, but constantly perform noise-driven transitions between the states. Thus, it will not be possible anymore to assign an end state to each set of initial conditions. Obviously, both transition rates, meaning from running to resting and in the opposite direction, will grow when the noise intensity D increases.

In addition to that, depending on the overall configuration, the system is usually biased towards one of the states. It is to be expected that at low bias current I , the resting state dominates and the running state is favored at high I . Considering the simulations (figure 8), this turns out to be a valid hypothesis: At $I = -0.1$, the neuron almost immediately returns to the resting state once it has gotten into the running state. At a slightly higher bias current of $I = 0$, the periods of stay in both states are almost equal, and at $I = 0.15$, the system is in the running state for the majority of time. The firing frequency in the running state lies at about 70 Hz.

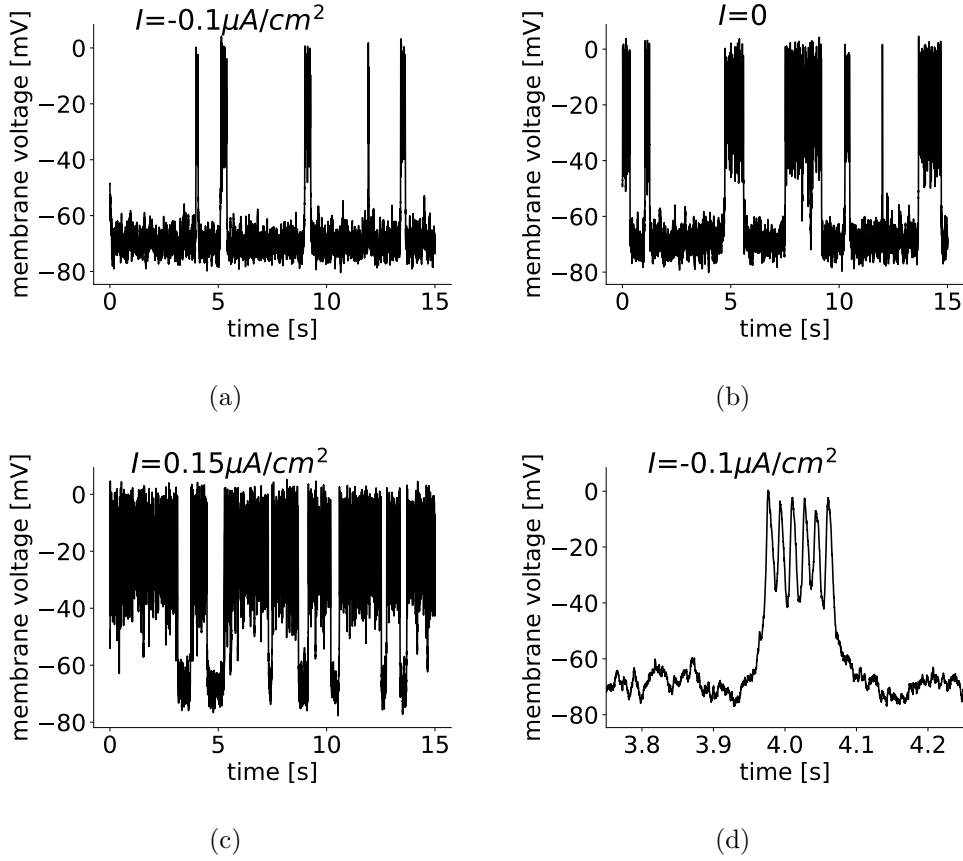


Figure 8: Behavior of the membrane voltage for constant noise and changing bias current I . In figure (d), a segment with a higher time resolution is shown in order to better illustrate the evolution of the voltage variable.

In conclusion, the behavior of this two-dimensional bursting model displays the same characteristics as the Brownian particle in a tilted potential. Therefore, we expect to find similar count statistics and Giant Diffusion for this system as well. If this assumption is actually valid will be examined in the following chapter.

2.1.3 System with periodic signal

2.2 $I_{Na,p} + I_K$ model with subcritical Andronov-Hopf bifurcation

If we observe Giant Diffusion in our simulations, it most certainly will not be restricted to only one neuron model. Therefore, it is of particular interest to possibly confirm this behavior also for other bistable two-dimensional neuron models. Finding out in which cases giant diffusion occurs may help to determine conditions that need to be fulfilled and eventually lead to experiments supporting these findings. Therefore two more models will be discussed in the following. The first one is again the $I_{Na,p} + I_K$ model. This model is very versatile and displays a wide variety of qualitative and quantitative behavior upon parametric adjustments. Thus, its features can be tweaked such that the system undergoes an Andronov-Hopf bifurcation when the bias current passes a certain value. As presented in section 3, the system is described by equations 6 and 7. The parameters now were the following:

$$C = 1, g_L = 1, E_L = -78, g_{Na} = 4, E_{Na} = 60, g_K = 4, E_K = -90.$$

Instantaneous Na^+ current:

$$k_m = 7, V_{1/2,m} = -30.$$

K^+ current:

$$k_n = 5, V_{1/2,n} = -45, \tau(V) = \text{const} = 1.$$

2.2.1 System without noise

Due to the parameter adjustments one obtains a slightly different phase space picture:

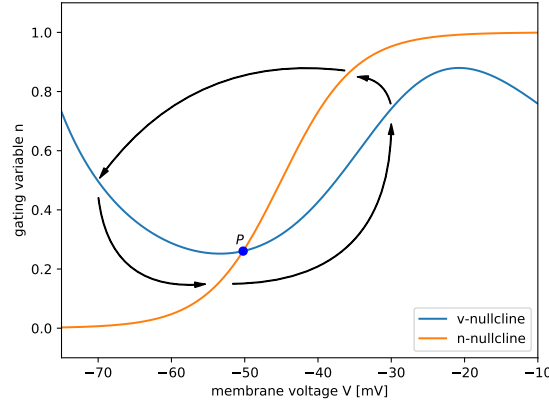


Figure 9: Nullclines of the adjusted $I_{Na,p} + I_K$ -model with $I = 46$. The arrows indicate the direction of motion in the different regions.

The new nullclines yield only one equilibrium point. Computing the Jacobian matrix, following eigenvalues arise for this point:

$$\lambda_+(P) \approx -0.05 + 2.3i \quad \lambda_-(P) \approx -0.05 - 2.3i$$

Complex eigenvalues with negative real parts indicate a stable focus. As before, the system performs large oscillations around the focus when it is in the running state. When it is near the equilibrium, it converges fast to it, with the exception that it doesn't approach it directly but oscillates around it with decreasing radius. In contrast to the previous case, the system now not only consists of stable limit cycle and equilibrium but also an unstable limit cycle in between the two stable configurations. Considering that the system is under the influence of noise, it will not spend much time in the unstable state and quickly collapse into a stable configuration.

Upon increase of the bias current, the unstable limit cycle shrinks. At $I \approx 48.9$, it falls together with the stable equilibrium and makes it lose stability. This transition is called a subcritical Andronov-Hopf bifurcation.

While in the first model the states were characterized by oscillations around different equilibria, the state vector now only rotates around one equilibrium point. The

current state can thereby be identified via the radius of the oscillations. Resting initial conditions result in a small radius and asymptotic convergence to the focus and spiking initial conditions just lead to regular firing with a larger radius, as can be seen in figure 10. Compared to the first model, the spiking limit cycle is not an ellipse anymore but displays some irregularities.

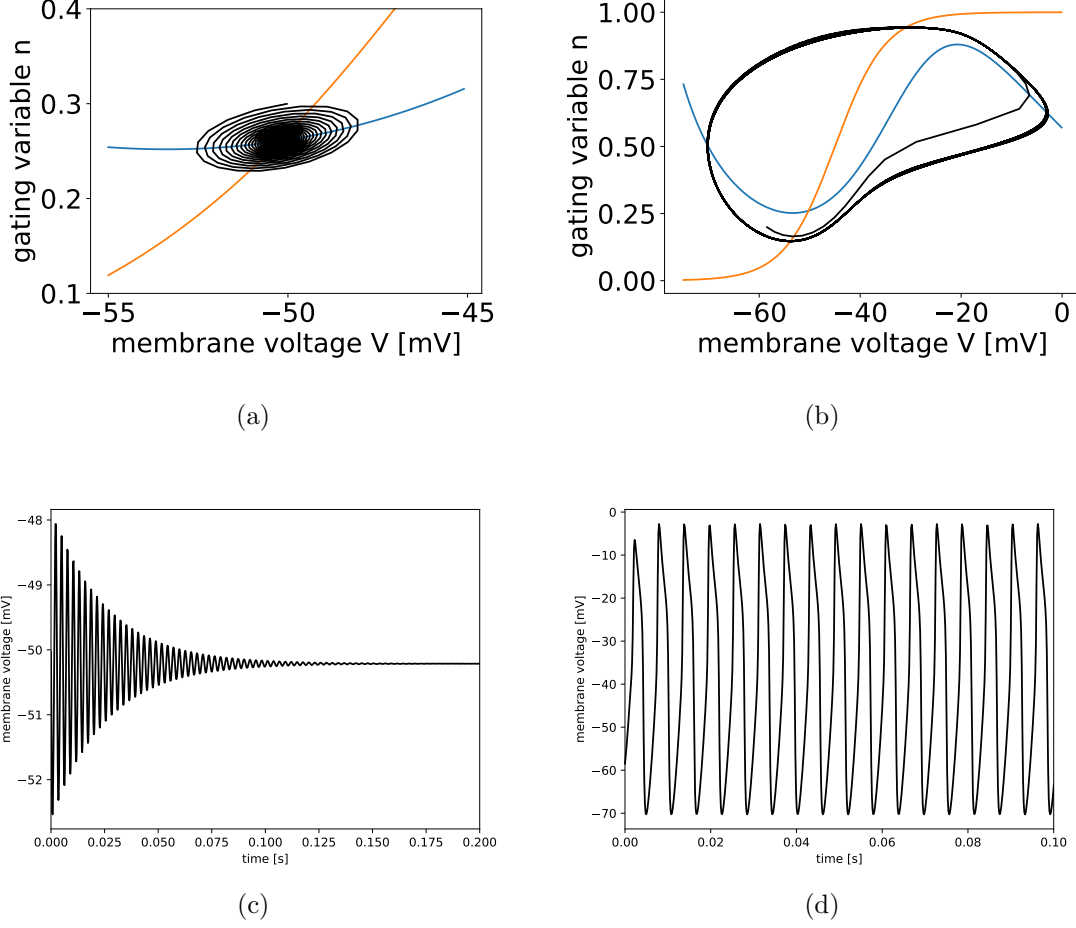


Figure 10: Evolution of the phase vector (first row) and the membrane voltage over time (second row). The left side shows the evolution of the system with resting ICs, and on the right one can see the behavior under spiking ICs.

In order to be able to distinguish between spiking and resting initial conditions, one may simulate the system at different starting points and see how it evolves, as has been done in section 2.1.1.

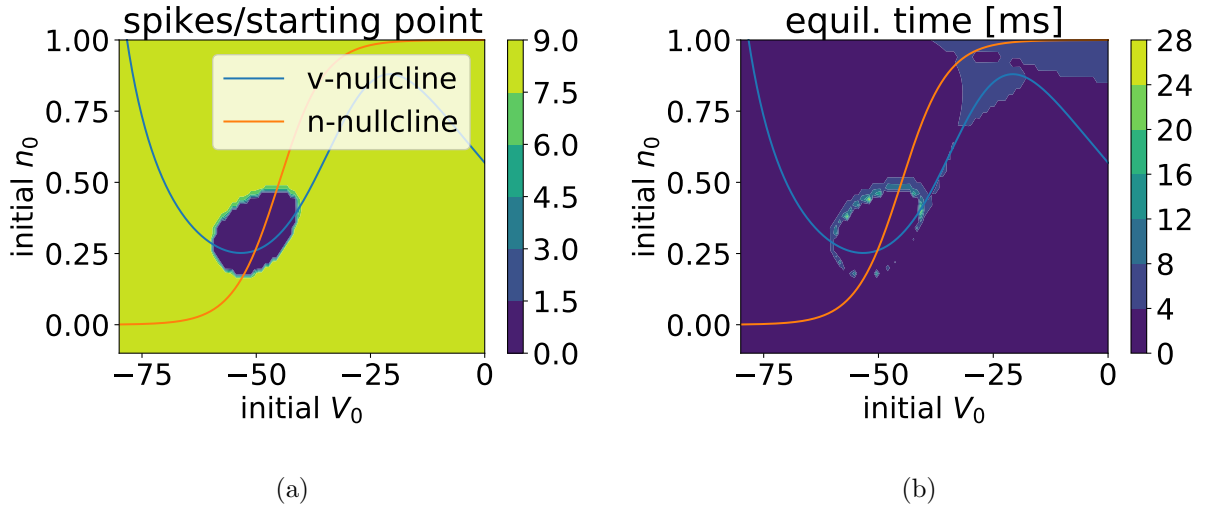


Figure 11: Phase plane image of the neuron model with $I = 46$ and no noise. Each point represents a specific combination of starting parameters. The left plot shows the number of spikes over a short period of time and for the right picture, the equilibration times for both states were measured. In both images one can see the shape of the unstable limit cycle that separates both domains. Irregularities arise from the finite resolution of the V_0 - n_0 -lattice.

The area of resting initial conditions is completely enclosed by the spiking regime. Near the border, the system takes longer to equilibrate. This is due to the unstable limit cycle which separates both regimes. By crossing this ellipse from within or from the outside, the system goes over into the firing or resting state, respectively. The course of the unstable limit cycle can be seen in figure 12. These images were obtained by simulating the neuron model with negative time steps. That way, unstable regions are turned into stable ones and vice versa.

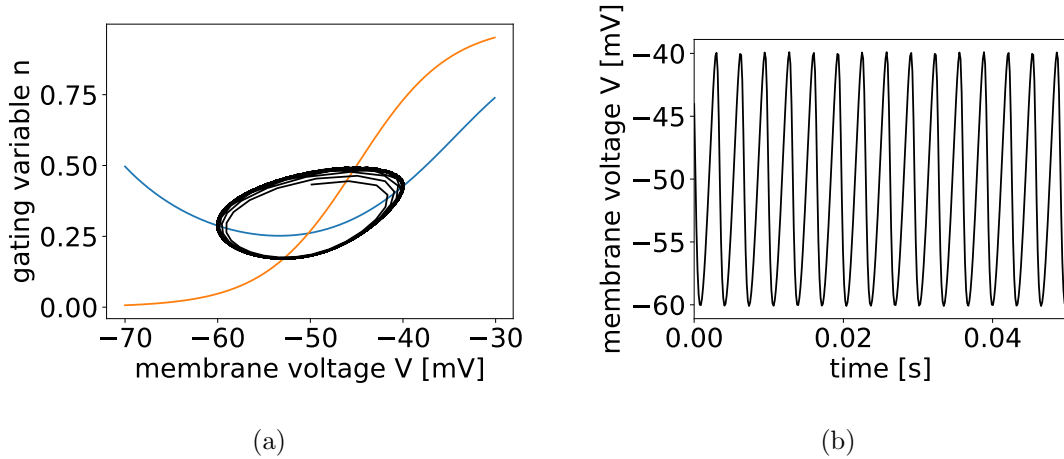


Figure 12: Evolution of the system on the unstable limit cycle. The left side shows the phase plane picture and on the right one can see the membrane voltage over time.

Due to the numerical impossibility to put the system exactly onto the unstable limit cycle, any time-forward simulation starting on the unstable cycle will eventually collapse into either stable configuration, as shown in figure 13.

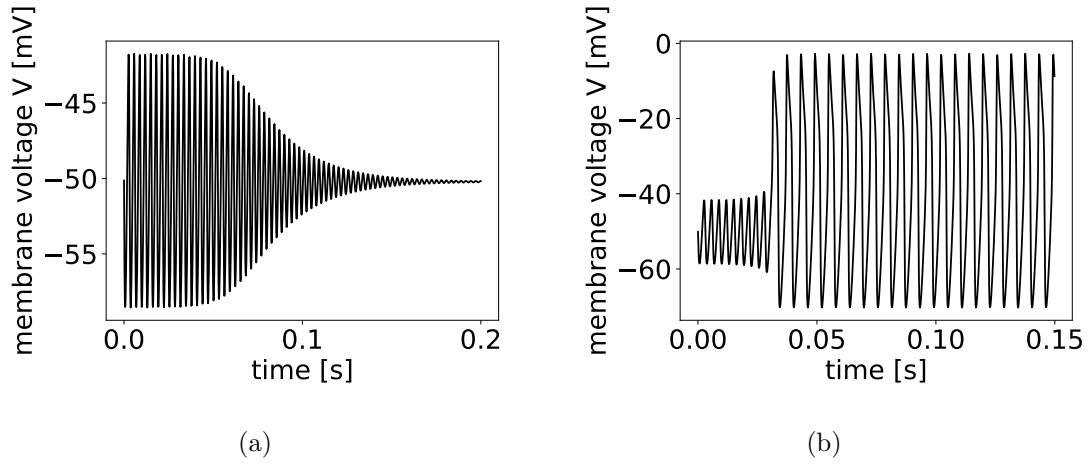


Figure 13: Evolution of the membrane voltage if the system is started near the unstable limit cycle. After a couple of circulations, the system quickly converges to a stable state.

2.2.2 System with noise

Considering that even in the noiseless system, the unstable limit cycle only lasts a few ms, it will not play any role in the noise-driven neuron. Therefore, the noise again just switches the system between spiking and resting state. The probability of each state can be influenced by tuning the bias current I , as can be seen in figure 14.

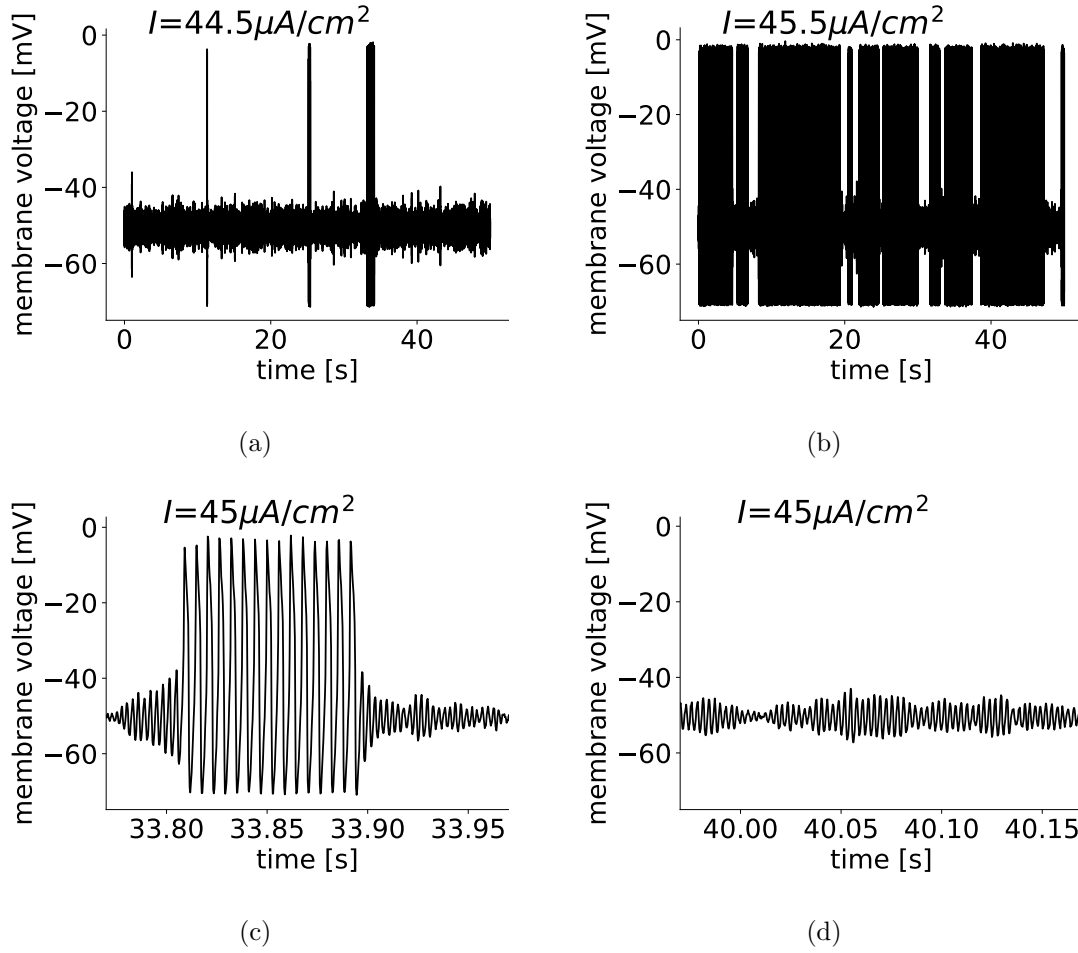


Figure 14: Behavior of the membrane voltage for constant noise and changing bias current I at $D = 0.3$. On the bottom, one can see the behavior of the system with a higher time resolution. The small oscillations near equilibrium in (d) are subthreshold oscillations.

Over a range of $1 \mu\text{A}/\text{cm}^2$, the neuron switches from barely spiking to basically only spiking. Due to the oscillatory properties of the system, small disturbances suffice to induce a change of state, if they occur at the right moment, as can be seen in 13 (c): Even though the state vector should be attracted to the stable focus, appropriate noise can slowly increase the amplitude of rotation until the spiking limit cycle is reached. In connection to this there exists another interesting phenomenon which is visible in (d): If the pulse amplitude is too small to make the neuron spike, it oscillates back to the focus with a high frequency. These subthreshold oscillations are a general characteristic of neurons with oscillatory potentials.

2.3 Rinzel model

The last model is a two-dimensional approximation of the Hodgkin-Huxley model, proposed by Rinzel in 1985 [19]. By assuming instantaneous Na^+ dynamics and expressing the two gating variables h and n by a single recovery variable W , Rinzel got the following model:

$$\begin{aligned} C\dot{V} &= I - g_{\text{Na}}m_{\infty}^3(V)(1-W)(V - E_{\text{Na}}) - g_{\text{K}}(W/S)^4(V - E_{\text{K}}) - g_{\text{L}}(V - E_{\text{L}}) \\ \dot{W} &= [W_{\infty}(V) - W]/\tau(V) \end{aligned}$$

It has to be noted that for our simulations, white gaussian noise with intensity D was added to the first equation. However, the notation is almost similar to the $I_{Na,p} + I_K$ model: I denotes again the bias current, C the capacitance, V the membrane voltage, g_i are conductances, E_i the Nernst equilibrium potentials and m_∞ the activation variable of the instantaneous Na^+ current. Inactivation of Na^+ and activation of K^+ are both governed by W . Its steady-state activation function W_∞ is a linear combination of n_∞ and h_∞

$$W_\infty(V) = S(n_\infty(V) + S[1 - h_\infty(V)]) / (1 + S^2)$$

and τ comes from averaging the time constants of the gating variables

$$\tau(V) = \frac{5 \exp[-(V + 10)^2/55^2] + 1}{3.82}$$

The parameters were taken from the original Hodgkin-Huxley model:

$$C = 1, g_L = 0.3, E_L = 10, g_{Na} = 120, E_{Na} = 115, g_K = 36, E_K = 12.$$

S can be obtained from the resting values of h and n

$$S = \frac{(1 - h_\infty(0))}{n_\infty(0)} = 1.27,$$

and

$$k_\infty = \frac{\alpha_k}{\alpha_k + \beta_k}$$

with

$$\begin{aligned} \alpha_n(V) &= 0.01 \frac{10 - V}{\exp\left(\frac{10 - V}{10}\right) - 1} & \beta_n(V) &= 0.125 \exp\left(\frac{-V}{80}\right) \\ \alpha_m(V) &= 0.1 \frac{25 - V}{\exp\left(\frac{25 - V}{10}\right) - 1} & \beta_m(V) &= 4 \exp\left(\frac{-V}{18}\right) \\ \alpha_h(V) &= 0.07 \exp\left(\frac{-V}{20}\right) & \beta_h(V) &= \frac{1}{\exp\left(\frac{30 - V}{10}\right) + 1} \end{aligned}$$

2.3.1 System without noise

The first step in the phase plane analysis would again be determining the nullclines. Unfortunately, the variable W not only appears linearly, but also in 4th power. This makes it analytically difficult to find a simple equation for the nullclines. Therefore, the nullclines were determined numerically:

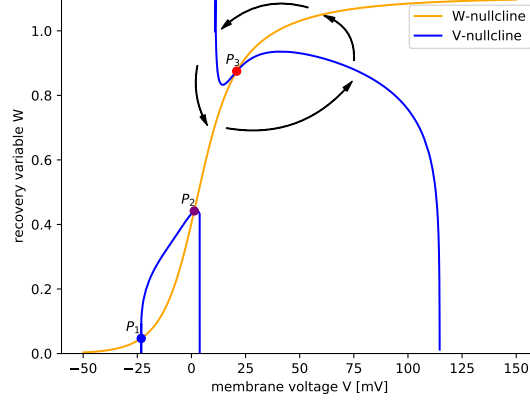


Figure 15: Nullclines of the Rinzel model with $I = -10$. The arrows indicate the direction of motion in the different regions.

Considering that this model is not a genuine two-dimensional neuron model, but just the result of a couple of simplifications carried out on the Hodgkin-Huxley model, the phase plane image can be understood as the 2-D projection of the 4-dimensional Hodgkin-Huxley model. Therefore, it comes as no surprise that the nullclines take on a more complex shape, consisting of a hill and an n-shaped part, both separated by a singularity at $V = 10\text{mV}$. However, this does not change the fact that there are still 4 regions of different directions of motion, which are marked by arrows in figure 15.

The numerical evaluation of the Jacobian matrix yields:

$$\begin{array}{ll} \lambda_+(P_1) \approx -0.3 & \lambda_-(P_1) \approx -0.7 \\ \lambda_+(P_2) \approx 0.5 & \lambda_-(P_2) \approx -1.4 \\ \lambda_+(P_3) \approx 6.3 & \lambda_-(P_3) \approx 0.5 \end{array}$$

This means that there is a stable node at P_1 , a saddle at P_2 and an unstable node at P_3 . Upon increase of I , the hill will move downwards, eventually leading to a merger of P_1 and P_2 at $I \approx -5.91$ when the system undergoes a saddle-node bifurcation and is no longer in the bistable regime.

When it is in the bistable regime, there are two sets of initial conditions, leading either to quiescence or repetitive firing as shown in figure 16.

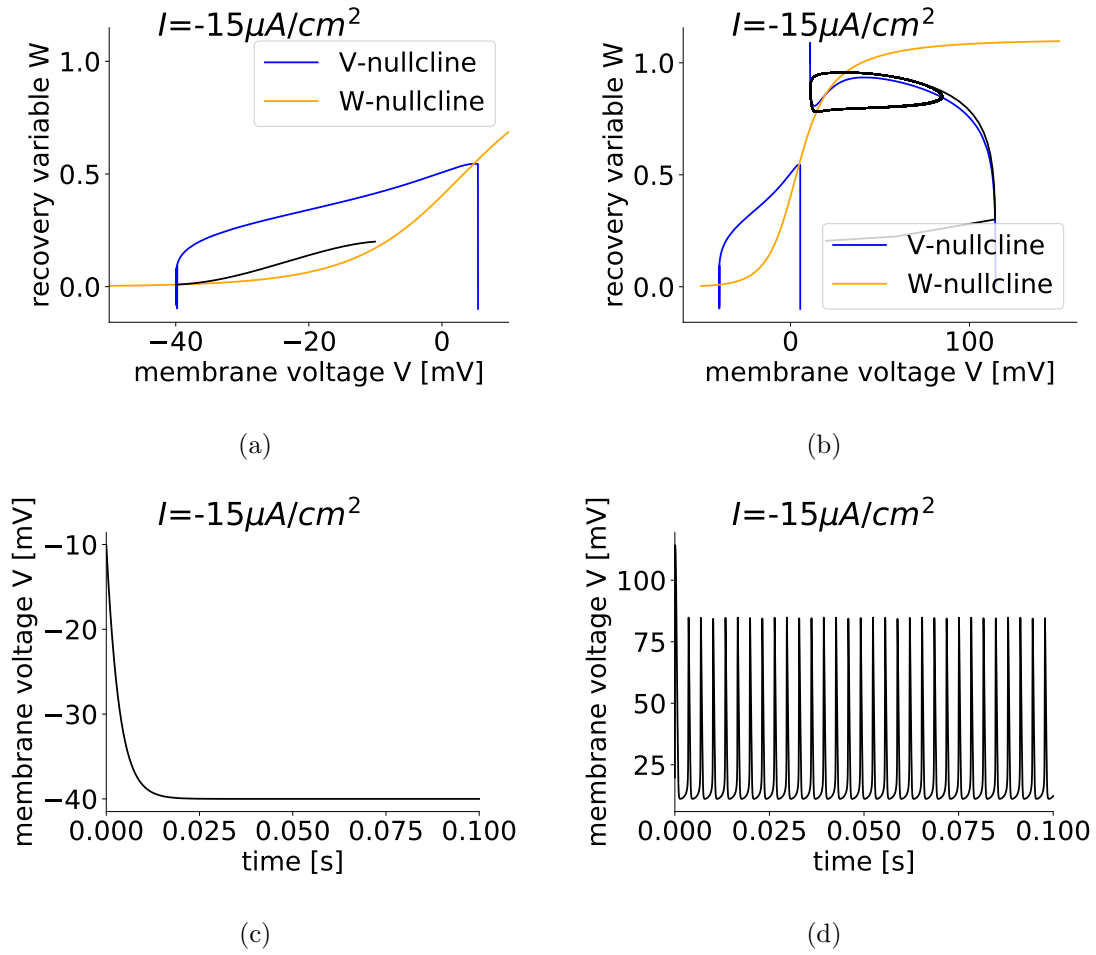


Figure 16: Evolution of the phase vector (first row) and the membrane voltage over time (second row). The left side shows the evolution of the system with resting ICs, and on the right one can see the behavior under spiking ICs.

Apparently, it is only a matter of a couple tens of microseconds to reach a stable configuration: the system converges exponentially to the stable equilibrium or after an initial spike, it goes around on the spiking limit cycle, respectively. The two sets of initial conditions can once again be distinguished by letting the system evolve without noise from different starting points:

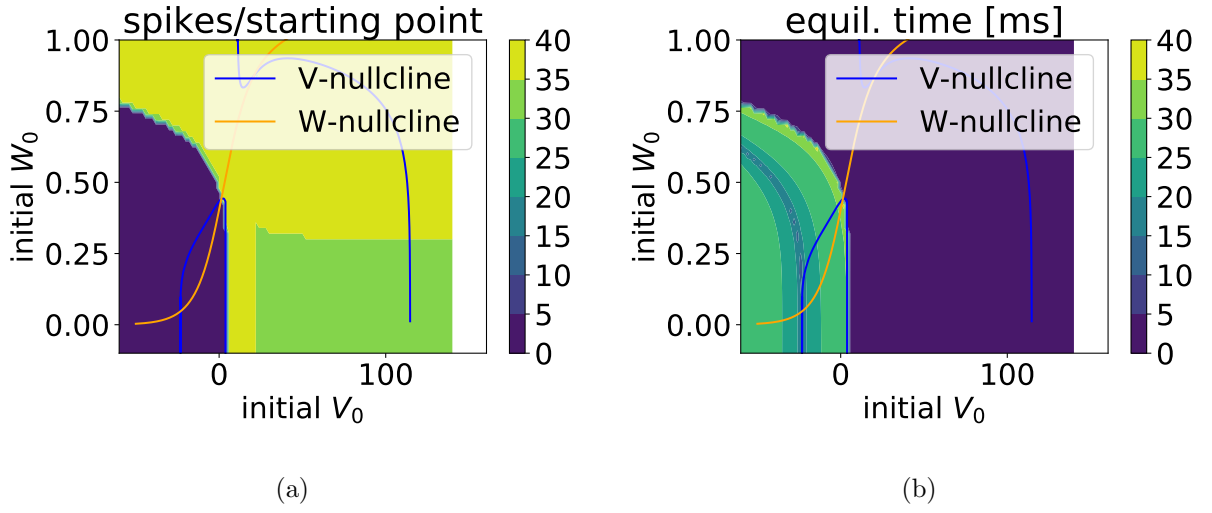


Figure 17: Phase plane image of the neuron model with $I = -10$ and no noise. Each point represents a specific combination of starting parameters. The left plot shows the number of spikes over a short period of time and for the right picture, the equilibration times for both states were measured. Irregularities arise from the finite resolution of the V_0 - n_0 -lattice.

Even though the nullclines have a more complex shape, the sets of initial conditions are again separated by a single line. Interestingly, the plots in figure 17 look inverse to each other. This means that the firing state is reached much faster than the resting state, almost independent of the starting point. Similarly to the $I_{Na,p} + I_K$ -model, the border goes, as expected, through the saddle point.

2.3.2 System with noise

Now that the model has been understood in the phase plane, the influence of noise can be investigated.

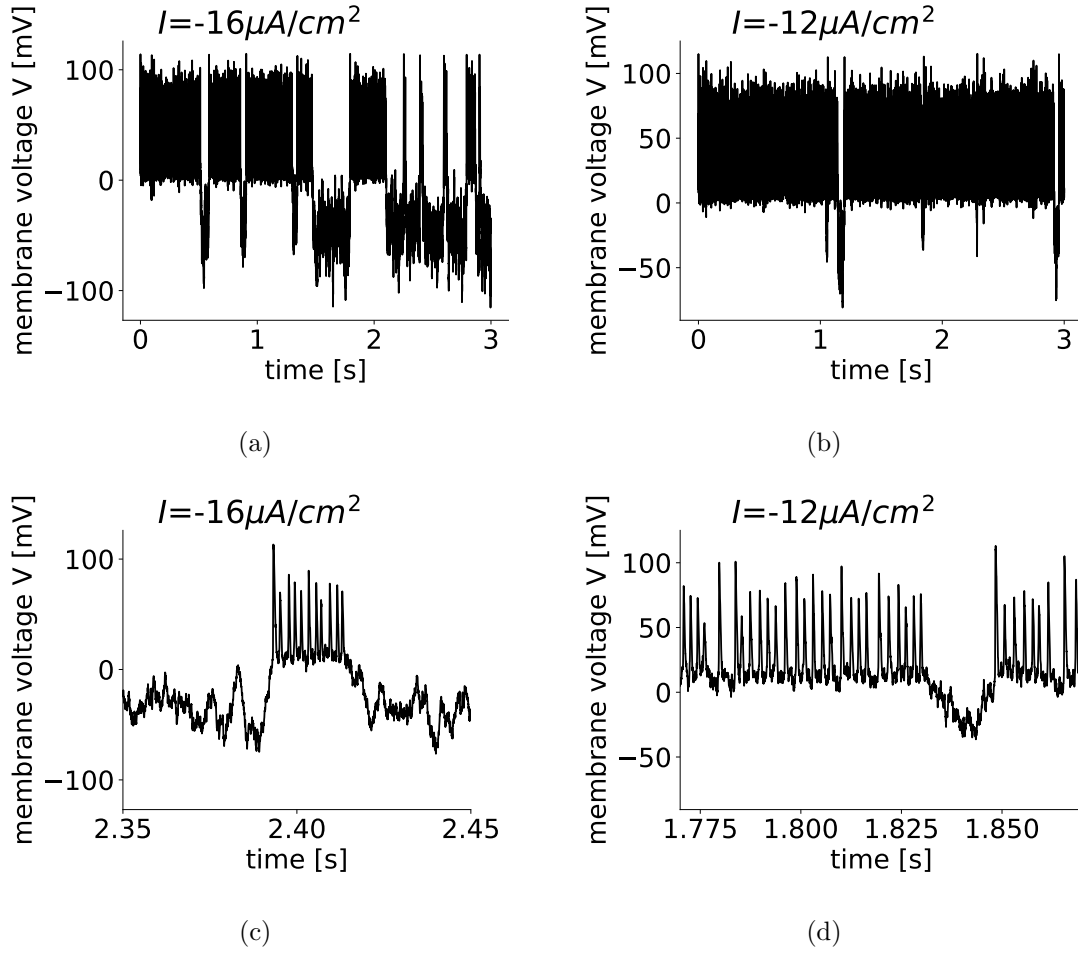


Figure 18: Behavior of the membrane voltage for constant noise and changing bias current I at $D = 100$. On the bottom, one can see the behavior of the system with a higher time resolution.

Here, too, the bias current I is the parameter that controls whether resting or spiking state is preferred. At intermediate I , the neuron fires irregularly and the noise has a high impact on its behavior. At high bias currents, the neuron barely goes into the resting state, and even that only for a short period of time before going back to tonic spiking. The major impact of noise in this regime lies in the modulation of firing rate and spike height, clearly visible in 18 (d).

2.4 Quantities of interest

2.4.1 System without signal

In the context of Brownian Motion, there were two characteristic quantities: the ensemble of particles moves with a mean velocity

$$\langle v \rangle = \lim_{t \rightarrow \infty} \frac{\langle x(t) - x(0) \rangle}{t} \quad (16)$$

and is subject to a diffusive spread around this average flow that can be described by the effective diffusion coefficient

$$D_{eff} = \lim_{t \rightarrow \infty} \frac{\langle x^2(t) \rangle - \langle x(t) \rangle^2}{2t} \quad (17)$$

In the context of neuron models, similar quantities can be defined. The most important event with regard to signal transmission is the generation of a spike. Therefore, it is often useful to approximate the voltage curve by a spike train where every spike is assumed to be a Dirac-delta function,

$$x(t) = \sum_i \delta(t - t_i) \quad (18)$$

The most relevant quantity is the spike count $N(t)$ which describes the number of spikes fired after a time t . This can be easily found by integrating the spike train over time:

$$N(t) = \int_0^t dt' x(t') = \sum_{t_i < t} 1 \quad (19)$$

Instead of the mean velocity, one can ask for the average firing rate

$$\langle v \rangle = \lim_{t \rightarrow \infty} \frac{\langle N(t) \rangle}{t} \quad (20)$$

and the diffusive spread of the spike count

$$D_{eff} = \lim_{t \rightarrow \infty} \frac{\langle N^2(t) \rangle - \langle N(t) \rangle^2}{2t} \quad (21)$$

A more common way to measure spiking variability in neurons is the Fano factor, which can be calculated by dividing the variance of the spike count by its mean value:

$$F = \frac{\langle \Delta N^2(t) \rangle}{\langle N(t) \rangle} = \frac{2D_{eff}}{\langle v \rangle}$$

2.4.2 System with signal

When bistable neurons are subjected to a periodic stimulus, they should change their firing pattern accordingly. This is best visible in the power spectrum of the spike train,

$$S(f) = \lim_{T \rightarrow \infty} \frac{\langle |\tilde{x}|^2 \rangle}{T} \quad (22)$$

The quality of signal transmission is measured by the signal-to-noise ratio (SNR). The stronger the system changes its behavior in response to the signal, the higher should be the signal-to-noise ratio. It is calculated by comparing the spectral power at signal frequency f_s with the noise, i.e. the spectral power of the background,

$$SNR = \frac{S(f_s) - S_{bg}(f_s)}{S_{bg}(f_s)} \quad (23)$$

The background power can be obtained by averaging the spectral power of a couple of points near the signal frequency while excluding the signal frequency itself. In the case of a weak and very slow signal, some simplifications can be made. First, it can be assumed that apart from a peak at the signal frequency, the power spectrum looks similar to the unperturbed one, yielding $S_{bg}(f_s) = S_0(f_s)$. In the low-frequency-limit, this simplifies even further to $S_0(f_s) = S_0(0)$. Lastly, the susceptibility χ which quantifies the modulation of the firing rate can be approximated with the

derivative of the firing rate $\langle v \rangle$ by the control parameter, in our case this is the bias current I . All in all, one then gets

$$SNR = \frac{\epsilon^2 T}{4} \frac{|\chi(\omega)|^2}{S_0(\omega)} = \frac{\epsilon^2 T |d\langle v \rangle / dI|^2}{8 \cdot D_{eff}} \quad (24)$$

where ϵ is the signal amplitude and T the total simulation time.

2.5 Two-state theory

2.5.1 Fano factor in weak noise limit

In the introduction we were able to describe the firing behavior of the neuron by using an Arrhenius-like description of the transition rates:

$$r_{\pm} = r_{0,\pm} \exp\left(-\frac{\Delta U_{\pm}}{D}\right)$$

This allowed us to define the effective diffusion coefficient:

$$D_{eff} = \frac{v_0^2 r_+ r_-}{(r_+ + r_-)^3}$$

As mentioned before, the calculation of a Fano factor is a more common way to describe the spiking characteristics of a neuron. Therefore, we will examine whether the Fano factor displays similar features in the weak noise limit as the effective diffusion coefficient. As

$$F = \frac{2D_{eff}}{\langle v \rangle}$$

an expression for the average firing rate is required to compute the Fano factor. Taking into account that the firing rate is zero when the particle is in the locked state, one finds the following formula for the total mean firing rate:

$$\langle v \rangle = v_0 \frac{r_-}{r_+ + r_-}$$

Therefore

$$F = \frac{2v_0 r_+}{(r_+ + r_-)^2} = \frac{2v_0 r_{0,+} \exp\left(\frac{-\Delta U_+}{D}\right)}{\left(r_{0,+} \exp\left(\frac{-\Delta U_+}{D}\right) + r_{0,-} \exp\left(\frac{-\Delta U_-}{D}\right)\right)^2}$$

In the limes $D \ll 1$ there are again two solutions. For $\Delta U_+ > \Delta U_-$:

$$F = \frac{2v_0 r_{0,+}}{r_{0,-}^2} \exp\left(-\frac{\Delta U_+ - 2\Delta U_-}{D}\right) \rightarrow \Delta U_+ = 2\Delta U_-$$

as well as for $\Delta U_+ < \Delta U_-$:

$$F = \frac{2v_0}{r_{0,+}} \exp\left(-\frac{\Delta U_+ - 2\Delta U_+}{D}\right) \rightarrow \Delta U_+ = 0$$

The intersection point for $\Delta U_+ > \Delta U_-$ stays the same while at the other critical point the potential barrier from running to locked state needs to vanish. As the latter condition violates the requirements for the application of the two-state theory - because only one state would exist in this case - the second intersection point can't be determined via this two-state model.

2.5.2 Behavior of SNR

Formula (24) allows to compute the SNR from D_{eff} and the derivative of the firing rate. As the effective diffusion coefficient can already be expressed via the transition rates, only $d\langle v \rangle / dI$ is missing. This can be found as follows:

$$\begin{aligned} \frac{d\langle v \rangle}{dI} &= \frac{d}{dI} \left(\frac{v_0 r_-}{r_+ + r_-} \right) = \frac{v'_0 r_-}{r_+ + r_-} + \frac{v_0 r'_-}{r_+ + r_-} - \frac{v_0 r_- (r'_+ + r'_-)}{(r_+ + r_-)^2} \\ &= \frac{v'_0 r_-}{r_+ + r_-} + \frac{v_0 (r_+ r'_- - r_- r'_+)}{(r_+ + r_-)^2} \end{aligned}$$

The derivative of v_0 is already known from simulations of the noiseless system, and the derivatives of the rates are given by

$$r'_\pm = \frac{r'_{0,\pm}}{r_{0,\pm}} r_\pm - \frac{\Delta U'_\pm}{D} r_\pm = \left(\frac{r'_{0,\pm}}{r_{0,\pm}} - \frac{\Delta U'_\pm}{D} \right) r_\pm$$

Once again, the missing derivatives can now be calculated numerically.

2.6 Numerical implementation

2.6.1 Simulation parameters

The behavior of the two-dimensional neuron model can be investigated by conducting simulations with the parameters described above and evaluating the data in a couple different ways. The simulations were done by letting the system evolve almost freely with the only external influence being the white gaussian noise with intensity D .

In all of the computations, only a single neuron was simulated over a long period of time. The ensemble of neurons was created by cutting this long simulations into multiple segments. When investigating an ergodic system, this procedure ensures that the results are independent of the initial conditions if the simulation time is long enough. Furthermore, an ensemble of neurons would need to be equilibrated before starting any measurements so that the obtained results would be correct. This equilibration time can be omitted now, which saves some computation time.

In all of the cases, the spike train was cut into $n_S = 50$ segments, which corresponds to an ensemble of 50 neurons. Each segment was cut into $n_I = 10^5$ intervals of length T_I . At each of these timepoints the spike count was combined with the spike counts from all the other segments in order to determine the effective diffusion coefficient D_{eff} and the fano factor F . This means that these quantities were calculated as double sums over time and segment:

$$D_{eff} = \frac{1}{n_S} \sum_1^{n_S} \left(\frac{1}{n_I} \sum_{i=1}^{n_I} \frac{N^2(T_I \cdot i)}{2T_I \cdot i} - \left(\frac{1}{n_I} \sum_{j=1}^{n_I} \frac{N(T_I \cdot j)}{\sqrt{2T_I \cdot j}} \right)^2 \right) \quad F = \frac{2D_{eff}}{\langle v \rangle}$$

Obviously, the average firing rate follows from the quotient of spike count and time. The other relevant parameters are shown in table 1. Longer simulation times have been used for smaller noise intensities. The ranges of I have been chosen in such a way that they lie completely in the bistable regime. For a bias current outside of that regime, the system would not switch anymore between the states and therefore also not exhibit stochastic bursting, which is required for our investigations. The noise

parameter	$I_{Na,p} + I_K$ model with saddle-node bifurcation	$I_{Na,p} + I_K$ model with Andronov- Hopf bifurcation	Rinzel model
length of timestep	$5 \cdot 10^{-4}$	$5 \cdot 10^{-3}$	10^{-2}
number of timesteps	$4 \cdot 10^{10} - 10^{11}$	$5 \cdot 10^9 - 5 \cdot 10^{10}$	$5 \cdot 10^9 - 6 \cdot 10^{10}$
range of I	$[-0.08, 0.3]$	$[43.25, 48]$	$[-17.2, -9]$
range of D	$0.25 - 0.45$	$0.15 - 0.35$	$20 - 50$

Table 1: Parameters of the investigated models

intensities D were as small as practically feasible. At very low noise intensities, the number of transitions was too low to observe enough switchings even in week-long simulations and thereby lower limits for D were set.

The ideal timestep was determined by simulating the system in the running state without noise. If the timestep was too large, the spike count would keep changing until finally approaching a minimum or maximum value, as can be seen in figure 19. It can be argued, however, that in the presence of noise, there is no deterministic behavior. This means that possibly larger timesteps would give the same results.

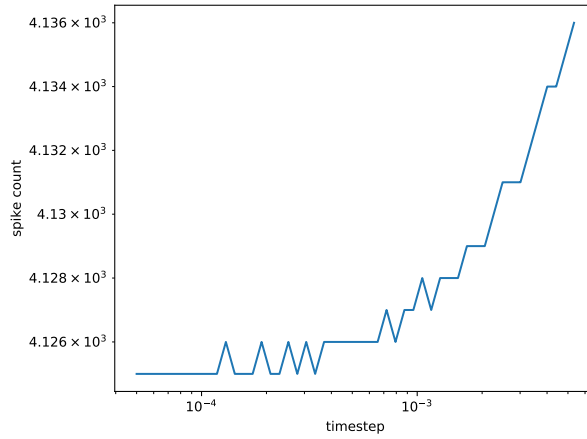


Figure 19: Determination of the ideal timestep for the $I_{Na,p} + I_K$ model. Shown is the deterministic spike count at different time steps.

2.6.2 Numerical subtleties

Obviously it is not useful to simulate neurons without getting any data from the computations. Therefore, multiple quantities were calculated and written out during the simulation of a neuron.

The most important event in the evolution of the neuron state vector is a spike. In order to be able to detect a spike, a reliable criterion needs to be found.

In the case of a system with saddle-node bifurcation off invariant cycle, a spike corresponds to a rotation of the state vector around the unstable equilibrium (not the saddle). This allows for a quite simple numerical criterion: every time the membrane voltage crosses the equilibrium value from below before the gating variable crosses its equilibrium value (also from below), a spike will be counted. Taking a look at the evolution of the membrane voltage, one might get the impression that just defining a voltage threshold would be enough to detect a spike. However, in the presence of noise, a neuron that is near the critical value can theoretically perform

infinitely many back-and-forth transitions over the threshold and thereby render an infinite - and unphysical - spike count. Consequently, a spike will only be counted after both thresholds have been crossed successively in the given order.

As mentioned before, the Two-State Theory allows us to describe our findings theoretically. As it is based on the transition rates between the states, it is important to be able to have a way to determine the state of the system. Clearly, the spiking state is characterized by repetitive firing. Thus, after having fired a spike, the neuron is considered to be in the spiking state.

In the resting state, the neuron state vector is in the vicinity of the stable equilibrium. This can be used to find a criterion similar to the detection of a spike: the neuron will be assumed to be in the resting state if membrane voltage and gating variable successively cross its stable equilibrium values. That way, one can ensure that it really has converged to the stable node and is not still in the intermediate area, where it may jump back any time.

Both criteria require the knowledge of stable and unstable equilibrium points. The stable equilibrium can be found by starting the simulation near the equilibrium and just letting the system evolve for a timespan much longer than the equilibration time. Luckily, also the unstable equilibrium can be found numerically. This was done by simulating the neuron with negative time steps. As mentioned before, this turns stable points into unstable ones and vice versa. Therefore, any simulation starting near the unstable equilibrium will then eventually end up there.

Considering that the neuron with subcritical Andronov-Hopf bifurcation shows slightly different phase space dynamics, the criteria needed to be adjusted. For the identification of the spiking state, a reference point was chosen between unstable and stable limit cycle, as far away as possible from the stable equilibrium. This point then again provided thresholds in both components which needed to be crossed in a successive order to count a spike.

In the resting state, the neuron would perform oscillations around the same equilibrium point, only with a smaller amplitude. Thus, a rectangle was drawn around the equilibrium, and once the oscillations stayed within this rectangle, it should have converged to the resting state.

The last aspect to take into consideration is the choice of initial conditions. As presumed, this has no influence on the overall course of the membrane voltage. Some results of simulations with different initial conditions are presented in the following section.

3 Critical currents in the Fano factor

3.1 Count statistics

3.1.1 $I_{Na,p} + I_K$ -model with saddle-node bifurcation

The first quantity to be considered is D_{eff} . As observed for the Brownian Particles, all curves intersect at two points whereby there is again a slight asymmetry, because the diffusion coefficient at the right intersection point is smaller than at the left intersection. These points define the range of Giant Diffusion: between the intersection points, decreasing noise intensity leads to increasing diffusion and outside of the critical region, less noise leads to smaller diffusion. Thus, for $D = 0.45$, the diffusion coefficient changes by approximately 3-4 orders of magnitude over the whole range

of bias currents I while the curve with $D = 0.25$ already extends over 6 orders of magnitude. If halving the noise intensity roughly doubles the order of magnitudes in the measured diffusion coefficient, the effects of further reductions will be even greater. This makes it numerically very difficult to go beyond the values chosen in this plot.

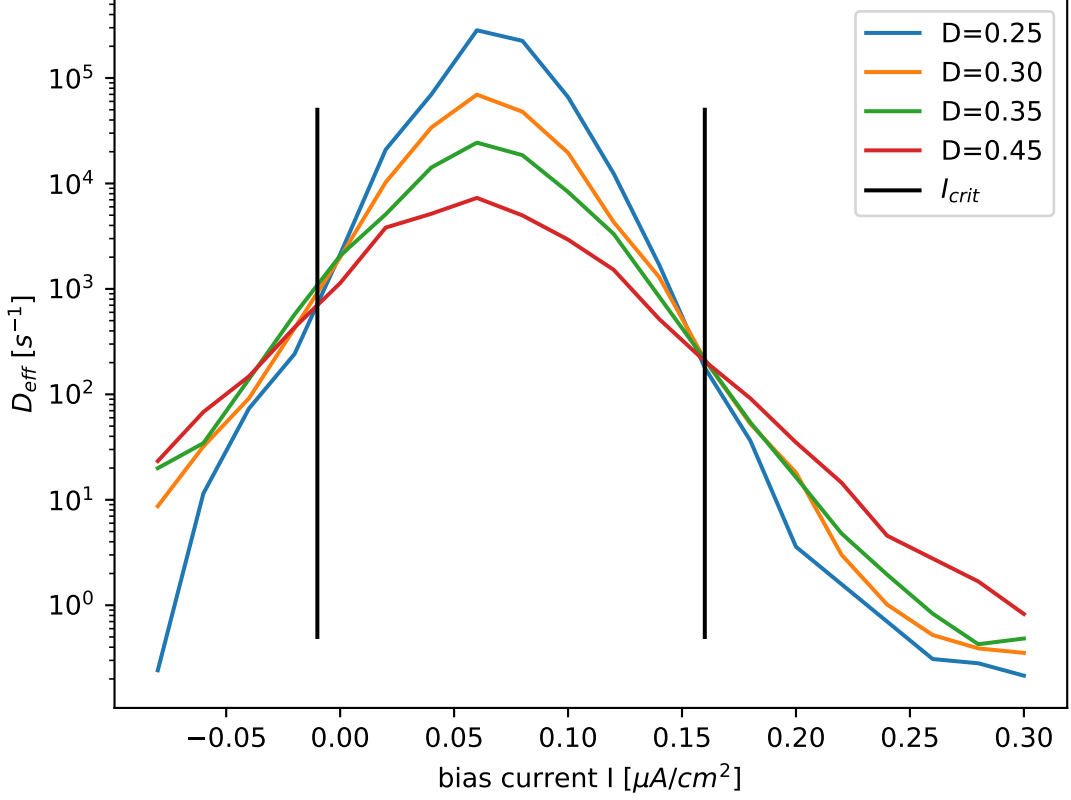


Figure 20: Effective diffusion coefficients for different noise intensities. The vertical lines mark the intersection points of the curves. The curve for $D = 0.25$ displays some irregularities at negative currents because the number of changes between both states was not high enough to yield good statistics.

The Fano factor looks slightly different than the diffusion coefficient: All curves only intersect at the right critical value of the current. This matches our prediction using the Two-State theory. Currents higher than this critical value lead to a decrease of F upon reduction of noise whereas at lower currents the Fano factor increases until it reaches a maximum. After the maximum, it steadily decreases. Even though the curve with the highest noise intensity spreads only over 4 orders of magnitude, F at $D = 0.25$ already spans 6 orders of magnitude, similar to D_{eff} at the same noise.

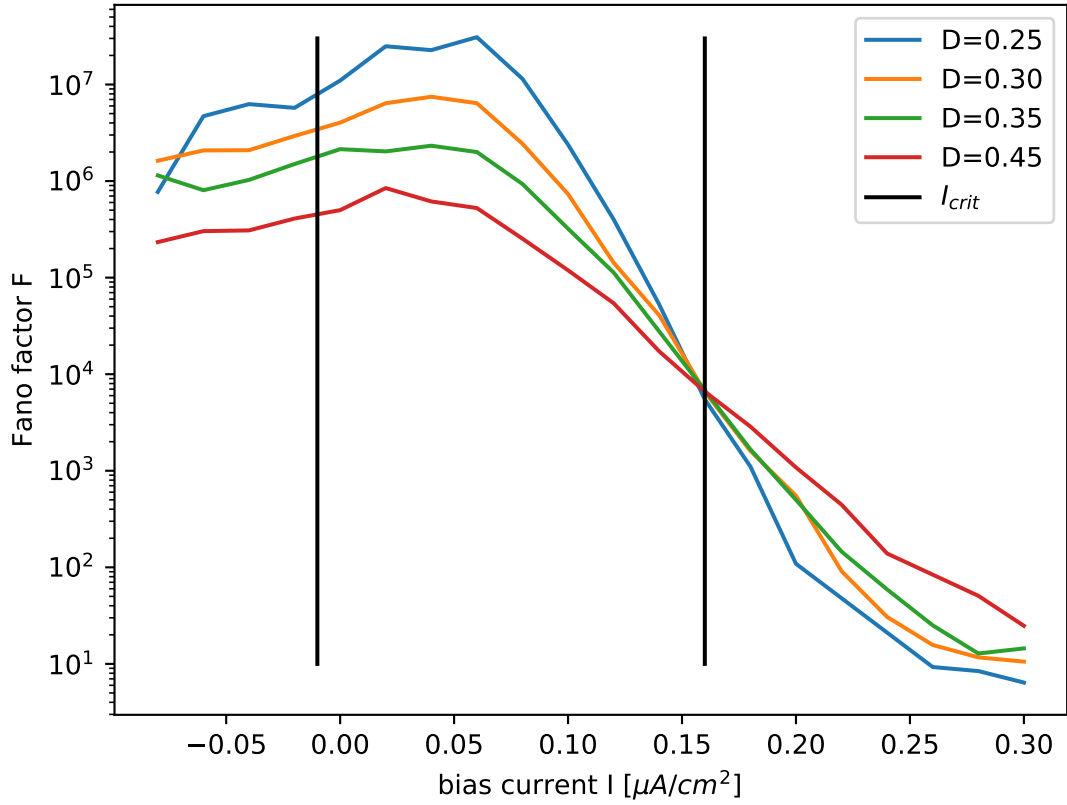


Figure 21: Fano factors for different noise intensities. The vertical lines mark the critical value of I determined from the curves of D_{eff} (Figure 20)

The mean firing rates start at zero, increase monotonically with the bias current and eventually approach the firing rate of the running state. This comes as no surprise considering that the neurons spend the majority of the time in the resting state at low bias currents and most of the time in the running state when I is high. All curves intersect at about $I = 0.08$, which roughly corresponds to the maxima of D_{eff} . This makes sense as the point where the system will be in either state with equal probabilities will also be the point where diffusion gets maximal.

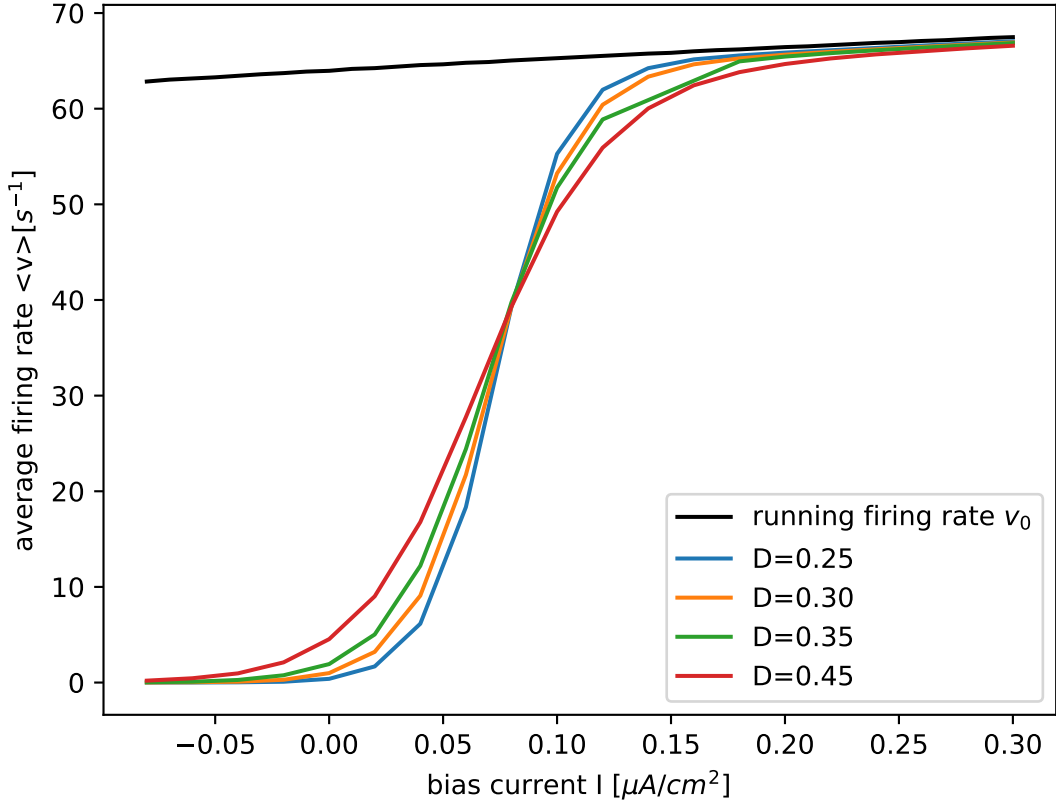


Figure 22: Average firing rates for different noise intensities. The black curve denotes the firing rate in the running state which was obtained from a simulation of the system without noise.

Finally, we can conclude that we observed Giant Diffusion in a two-dimensional neuron model. Now we need to find out whether there are different models exhibiting similar behavior.

3.1.2 $I_{Na,p} + I_K$ model with subcritical Andronov-Hopf bifurcation

Taking a look at the effective diffusion coefficient of our second model, some similarities to the first model become apparent. As before, all curves intersect at two points which define a region of Giant Diffusion: between these points, D_{eff} increases when the noise decreases, and outside of this region, the diffusion goes to zero. Interestingly, the curves are a little more asymmetric than before, as D_{eff} differs by more than one magnitude with regard to the other intersection point. Lastly, the diffusion coefficient at lowest noise D exhibits a growth of almost 8 orders of magnitude over the whole range of bias currents, which are two more orders of magnitude than before.

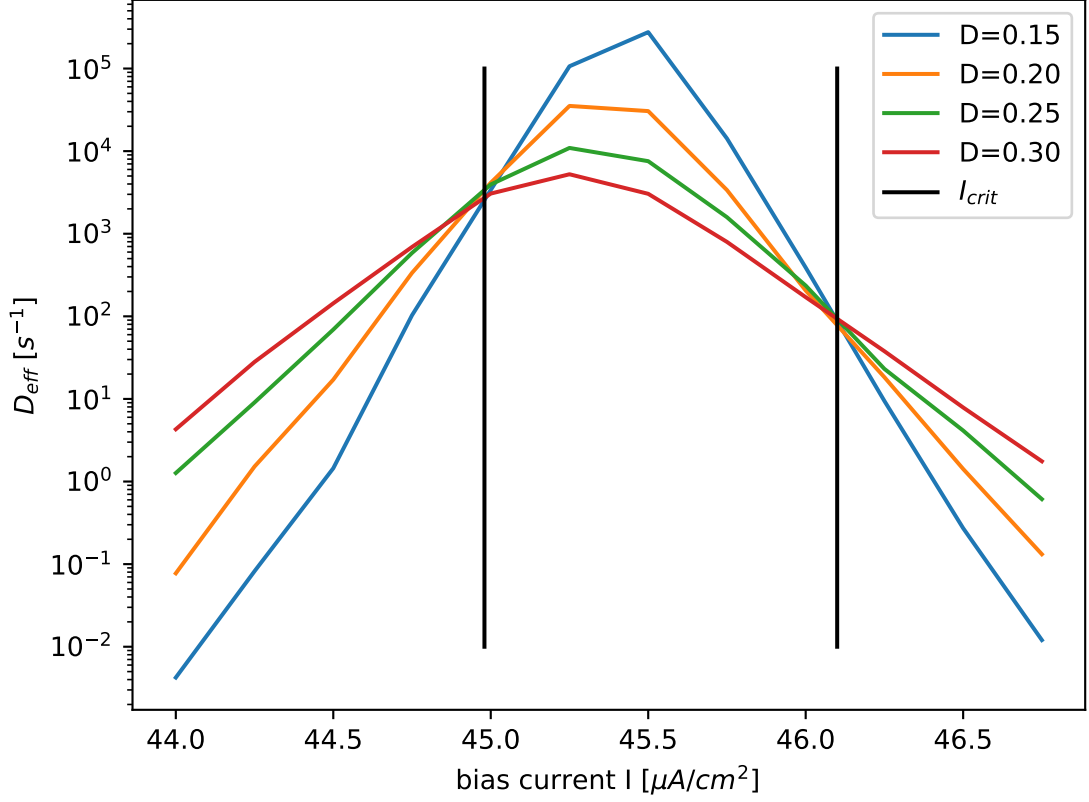


Figure 23: Effective diffusion coefficients for different noise intensities. The vertical lines mark the intersection points of the curves.

Next, we take a look at the Fano factor. Also here, in accordance with the Two-State theory, all curves have only one intersection point which corresponds to the right critical current. Furthermore, all curves have a maximum inside the region of Giant Diffusion. At lower bias currents I , the curves display a modest decrease up to 2 orders of magnitude. However, at bias currents right of the maximum, the Fano factor drops much steeper by up to 8 orders of magnitude in the shown range, similarly to D_{eff} .

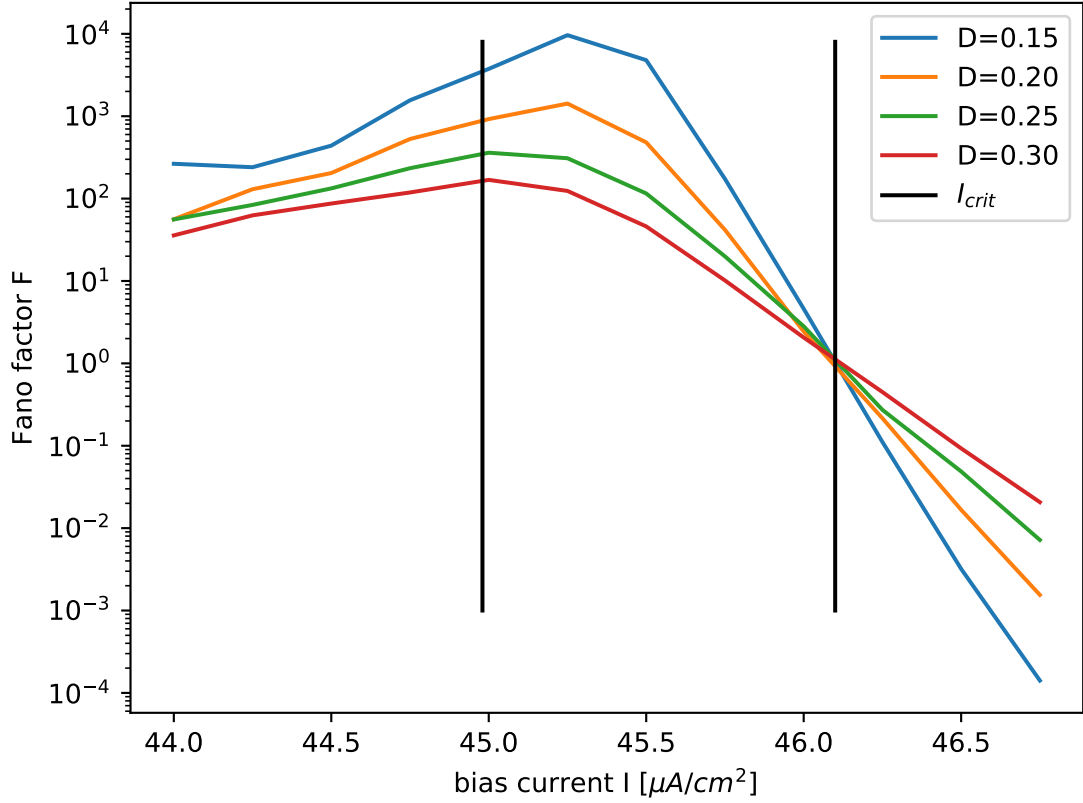


Figure 24: Fano factors for different noise intensities. The vertical lines mark the critical values of I determined from the curves of D_{eff} (Figure 23)

Lastly we investigate the overall firing rate. all curves monotonically increase, intersect and finally converge to the firing rate in the spiking state. Especially in this picture one can see the greater asymmetry of the second neuron model: while the curves for the first model looked point-symmetrical with regard to the intersection point, the intersection is now shifted towards a higher bias current. However, its position roughly matches the maximum of D_{eff} . This seems reasonable because in the limit of $D \rightarrow 0$, this would be the point where the neuron switches from resting to spiking activity, and therefore also the maximum of D_{eff} .

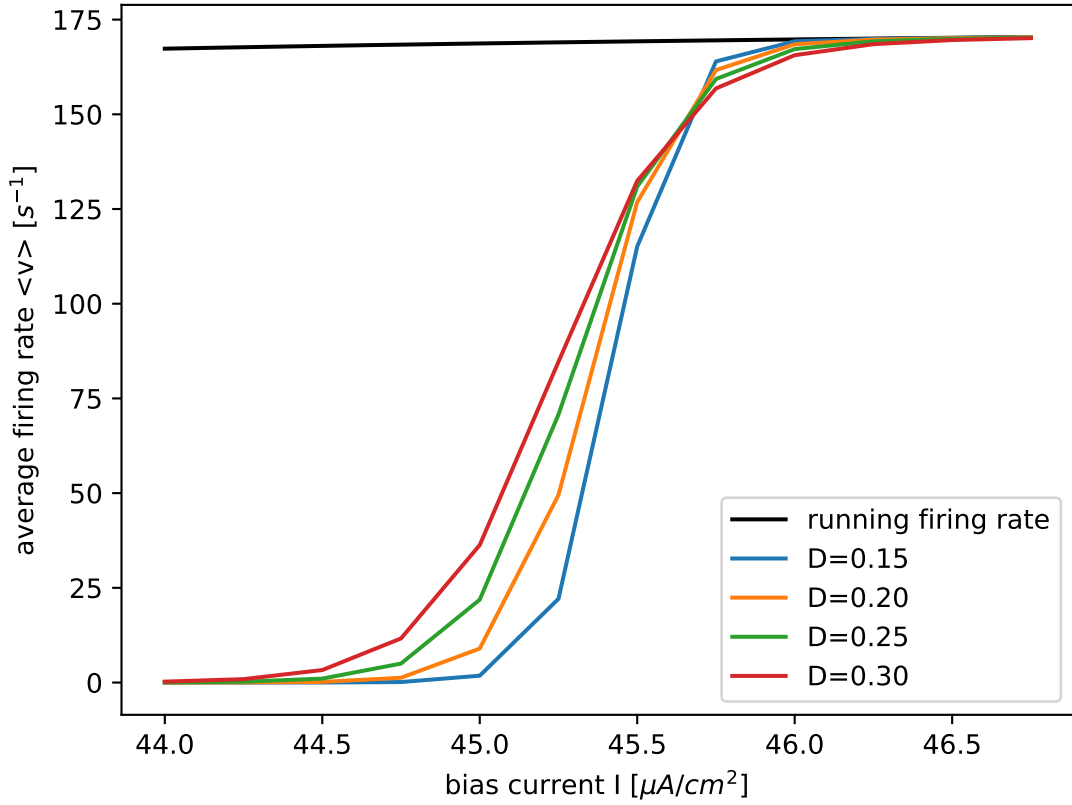


Figure 25: Average firing rates for different noise intensities. The black curve denotes the firing rate in the running state which was obtained from a simulation of the system without noise.

3.1.3 Rinzel model

Having observed Giant Diffusion in two variants of the $I_{Na,p} + I_K$ model, we will now answer the question whether the much more complex model proposed by Rinzel aligns with the simpler model. Once again we will start with the effective diffusion coefficient D_{eff} .

At first glance, the image does not look too different from the previous models. All curves have maxima in the simulated range of bias currents, and they share a sharp intersection point at around $I \approx -11$. However, there is no clear intersection on the left side, so defining two critical currents would be ludicrous. In addition, the maxima visibly shift to the right with decreasing noise. This might suggest that the chosen noise intensities are still too far away from the low noise limit which is a requirement for sharp intersection points. Nevertheless, the diffusion coefficient increases with decreasing noise between the intersections, and decreases outside of this region, resulting in changes of 5 orders of magnitude. Consequently, Giant Diffusion exists also in this model.

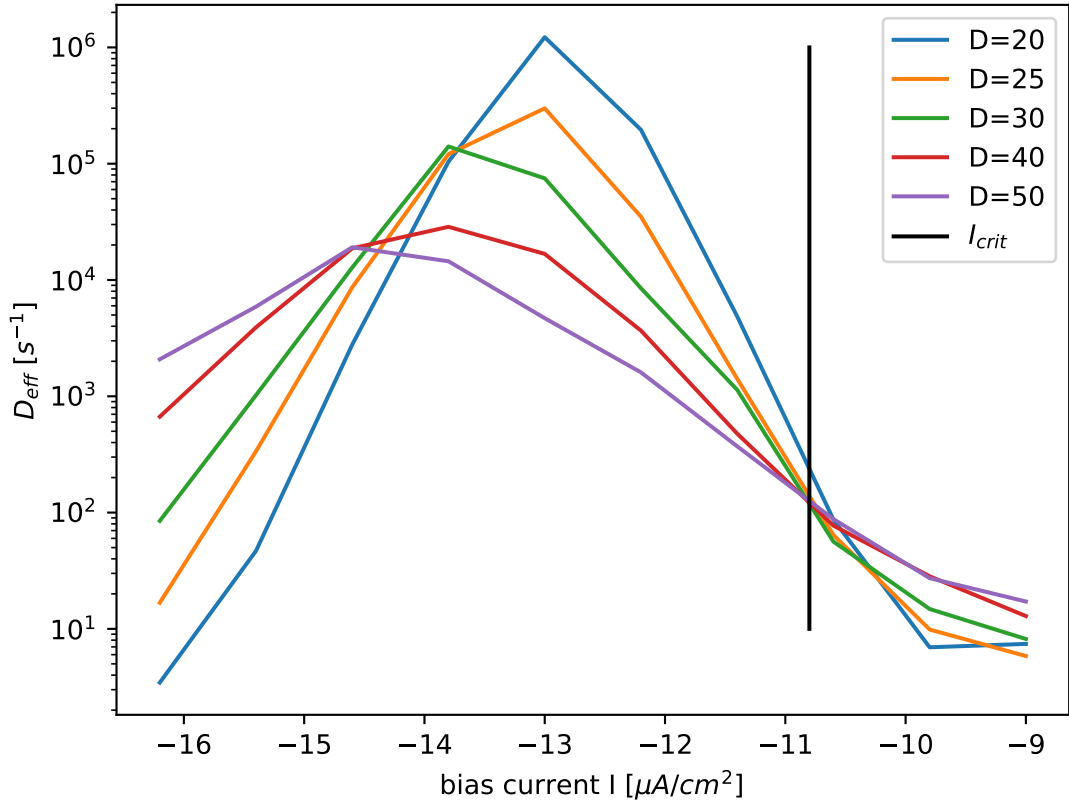


Figure 26: Average firing rates for different noise intensities. As the firing rate in the spiking state depends on the noise intensity, the reference curves were omitted for the sake of clarity.

The fano factor looks almost similar to the $I_{Na,p} + I_K$ model. The curves intersect at the critical current, decrease left of it and increase right of it until they reach a maximum and start to slowly decline. As in D_{eff} , the overall change amounts to up to 5 orders of magnitude.

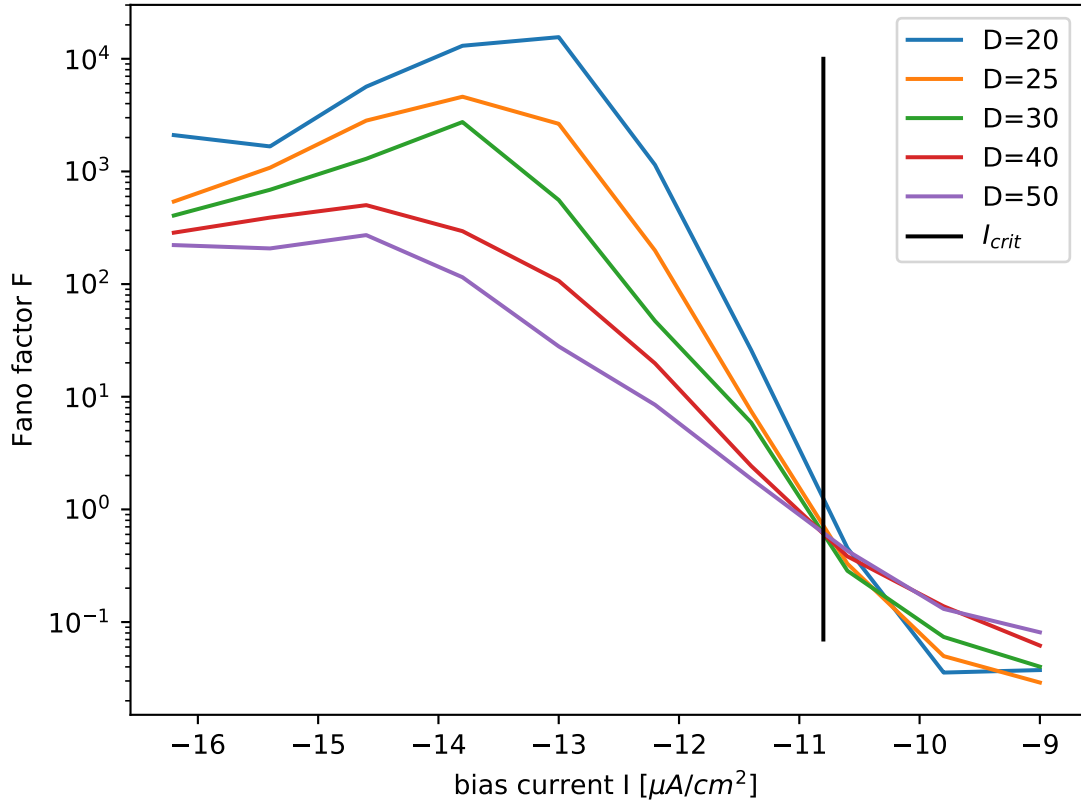


Figure 27: Fano factors for different noise intensities. As the firing rate in the spiking state depends on the noise intensity, no reference curves could be determined.

Finally, we will once again investigate the overall firing rate. All curves increase monotonically with the bias current I and finally approach a value of around 400 Hz. Strangely however, they never intersect. This has to do with the firing rate in the spiking state which exhibits a noise-dependence, meaning that higher noise leads to faster firing. For the first model, a short simulation of the undisturbed (noise-free) system yielded a reference value for the firing rate in the spiking state. This is now not possible anymore. Instead, one can simulate the models with noise, count the spikes and divide this by the total time in the spiking state. The results from these simulations agree well with the measurements shown here.

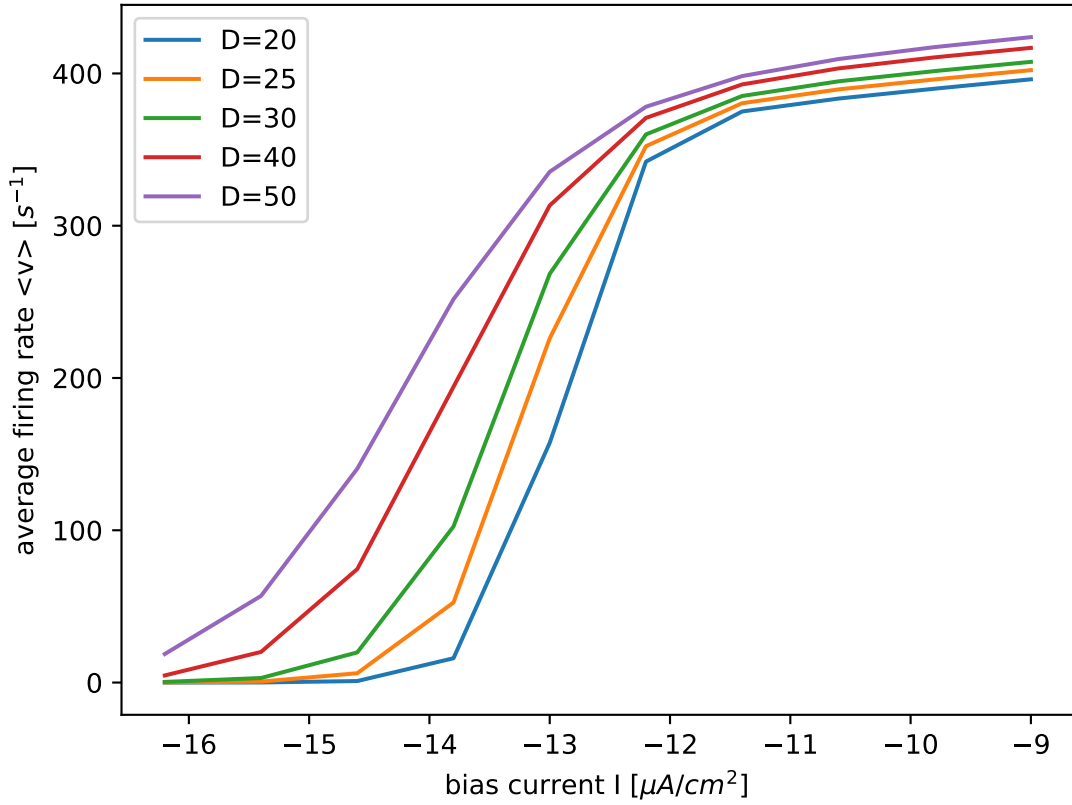


Figure 28: Average firing rates for different noise intensities. As the firing rate in the spiking state depends on the noise intensity, the reference curves were omitted for the sake of clarity.

3.1.4 Influence of the initial conditions

We mentioned before that the choice of initial conditions should in theory not have any influence on the results, if the simulations were long enough. In order to confirm this numerically, some measurements were conducted with the Rinzel model under different initial conditions. The results of these measurements are shown in figure 29. It is apparent that the curves of the effective diffusion coefficient D_{eff} as well as the average firing rate $\langle v \rangle$ nearly overlap and are basically similar. Thus, it can be said that for the chosen set of simulation parameters we can start at any point in the phase space without having to worry about the plausibility of our results. Nonetheless it is important to keep in mind that this only holds if the system performs enough transitions between the states. Preferably, we would like to see at least 100 transitions, but it was found that a couple dozen transitions already ensure reliable statistics.

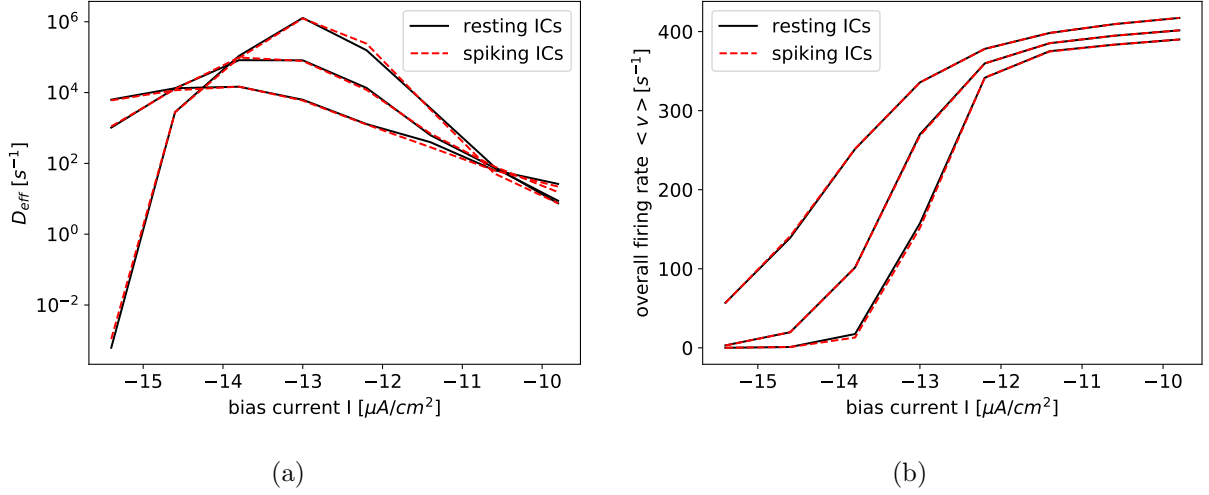


Figure 29: Simulations with starting and resting initial conditions. It can be clearly seen that the choice of starting parameters neither affects the effective diffusion coefficient nor the overall firing rate.

3.1.5 Conclusion

Examining 3 different two-dimensional bistable neuron models we have found Giant Diffusion in all of them. This implies that bistability between resting and repetitive firing is the only condition that needs to be fulfilled in order to observe this phenomenon in neurons.

4 Transition rates in bistable neurons

While the spike count may be the most important quantity to determine, there are some other characteristics which should be investigated. An example for these are the transition rates between the states which could allow us to describe our findings with the Two-State theory. Considering that we have seen some differences between the 3 neuron models, we will go into each one separately in this section.

4.1 $I_{Na,p} + I_K$ model with saddle node bifurcation

4.1.1 Distribution of the state lifetimes

The transition rate from one state into the other is inversely proportional to the amount of time the system stays in the first state: the longer it stays in one state, the smaller the transition rate to the other state. So, in order to find transition rates, we will investigate the statistics of the running and resting time intervals.

In the case of a high number of transitions, the equilibrium as well as the resting time intervals display a simple exponential distribution, indicating that the transitions are random and independent (figure 30). This is an important finding because it justifies just averaging the interval lengths in order to get average transition rates. If the distributions looked more complex, e. g. if they featured multiple extrema, this description might not be adequate anymore.

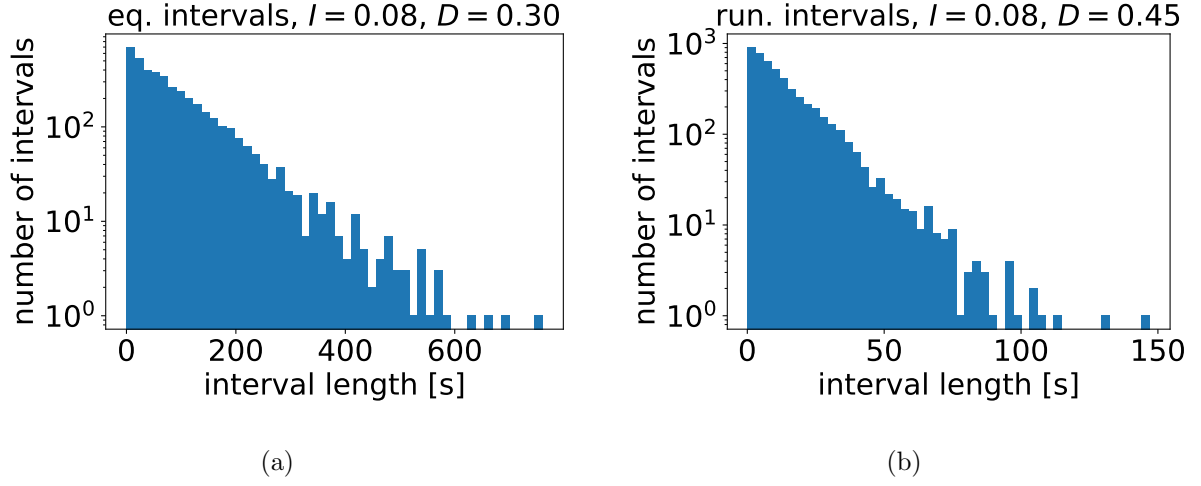


Figure 30: Distribution of equilibrium time intervals (left) and running time intervals at high switching rates

Depending on the noise intensity, the interval lengths can range from some seconds to a few minutes. As the number of events decreases with the interval length, the tail of the distribution gets less regular. Consequently, in the case of a small number of transitions, the whole distribution looks like the tails of the shown histograms.

4.1.2 Transition rates at different noise intensities

Due to the exponential (and thereby fast decaying) distribution of the resting and running intervals, one can now reasonably calculate transition rates.

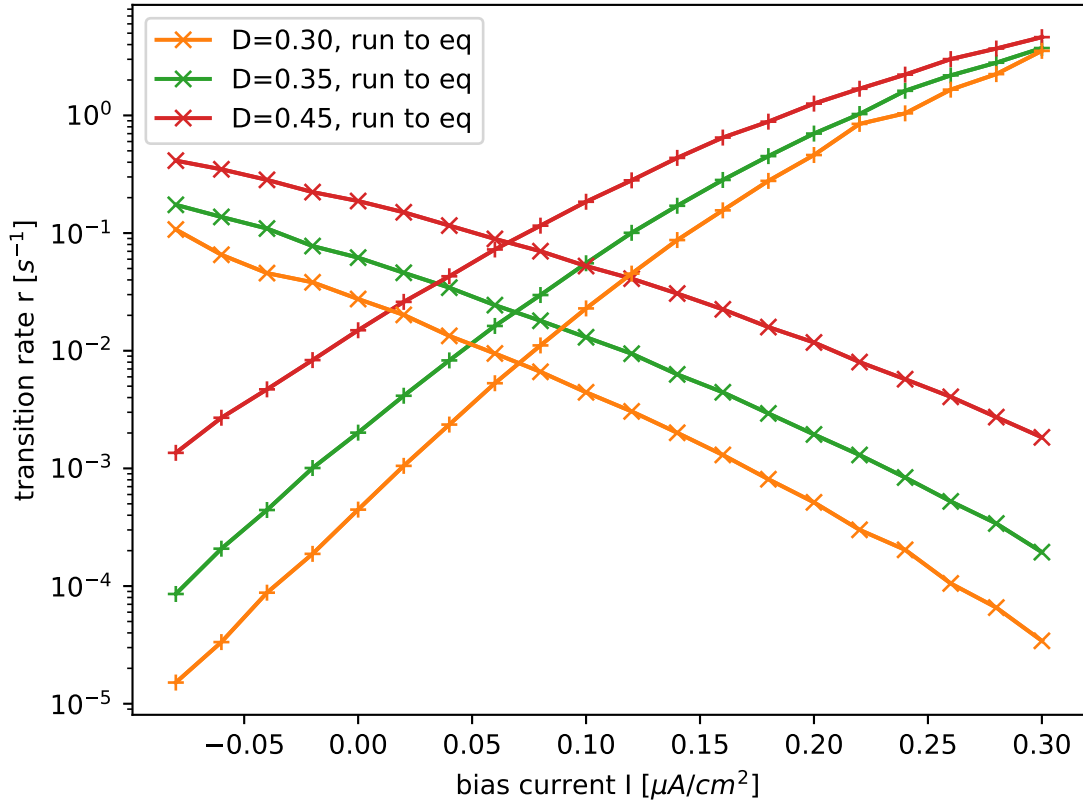


Figure 31: Transition rates between the states for a couple different noise intensities

As expected, the transition rates grow with the noise intensity. Furthermore, the transition rates from running state to equilibrium decrease with the bias current, while the rates of the opposite transition grow. What this basically means is that the higher the bias current, the higher the likelihood of getting into the running state and the longer are the residence times in this state, which is consistent with the phenomenology of the system. The last observation to discuss here are the intersection points of the rates at the same noise intensity. These can all be found at a bias current of about $0.07 \mu A/cm^2$, corresponding to the maxima of the effective diffusion coefficients in figure 20. Thus, diffusion gets maximal when the transition rates are of equal size and the system stays in both states equally long, which agrees with our understanding of the system.

4.1.3 Arrhenius Plots and effective potential barriers

For a given bias current, the transition rates can be put into an Arrhenius plot.

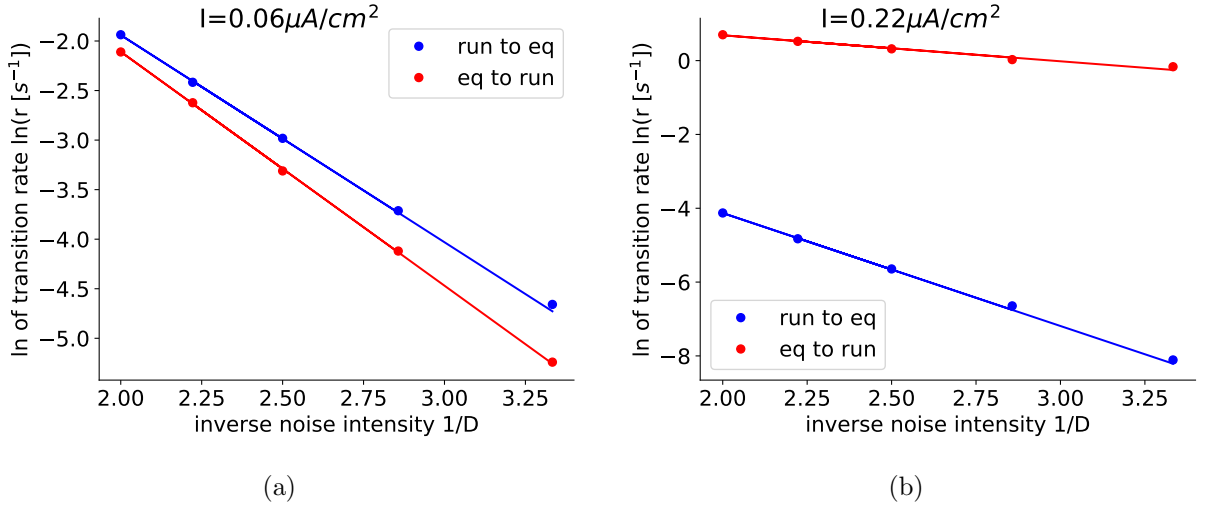


Figure 32: logarithm of the transition rates in the middle of the area with giant diffusion (a) and outside of it (b). The respective potential barriers arise from the slope of the lines.

The logarithmic plots illustrate the exponential dependence of the transition rates on the noise intensity at any given bias current. In order to extract effective potential barriers, these data were fit with functions of the form

$$r_{\pm} = r_{0,\pm} \exp\left(-\frac{\Delta U_{\pm}}{D}\right) \quad (25)$$

as introduced in section 2.5. Another possible way to fit the data would be to introduce a noise dependence into the prefactor in order to have a Kramers-like formula:

$$r_{\pm} = r_{0,\pm} D^{\alpha} \exp\left(-\frac{\Delta U_{\pm}}{D}\right)$$

This yields only slightly better results with regard to the R^2 value, so the simpler formula will be used for our calculations.

Assuming the functionality given in equation (25), the effective potential barriers can very easily be obtained by determining the slope of the lines in figure 32.

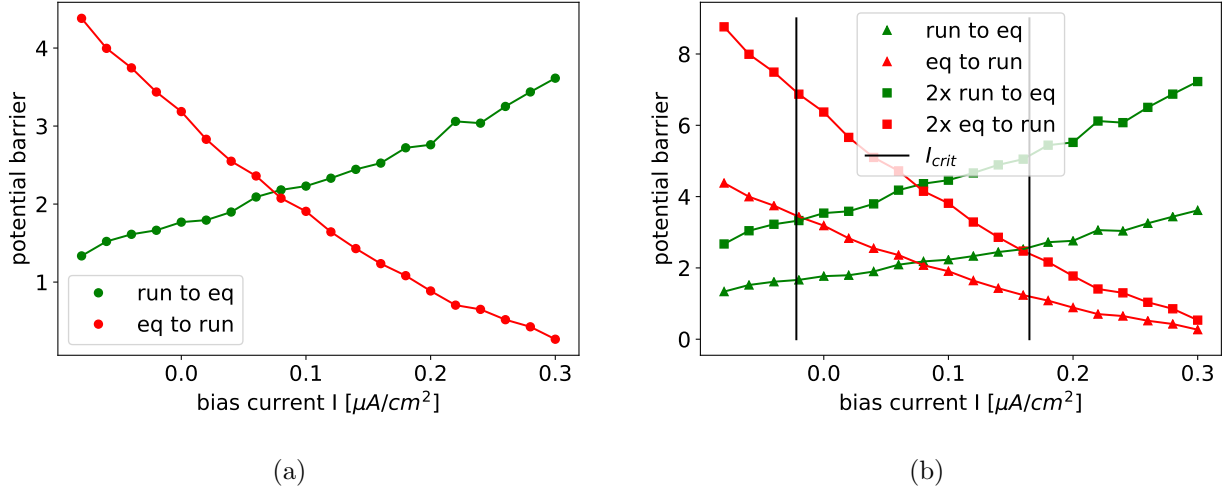


Figure 33: Effective potential barriers for both transitions. As the running state is favored at high bias currents, ΔU_+ increases, while the other one drops. The points where $\Delta U_i = 2\Delta U_j$ correspond to the numerically computed intersection points from figure 20 with only slight deviations.

The behavior of the potential barriers is consistent with the previous findings. The transition rates as well as the preference of the running state with rising I imply an increasing ΔU_+ and decreasing ΔU_- . The critical bias currents that are given by $\Delta U_i = 2\Delta U_j (i \neq j)$ are in accordance with the intersection points of the effective diffusion coefficients but are slightly offset outwards. This indicates that there are still some finite-noise effects present. In the limit $D \rightarrow 0$ it is to be expected that the diffusion coefficients intersect exactly at the critical bias currents given by the potential barriers.

4.1.4 Comparison with two-state theory

Having fits of the transition rates available allows us to compare the measured curves with the two-state theory and try to make predictions for other noise intensities. As mentioned before, calculating the relevant quantities merely requires knowledge of the transition rates r_{\pm} and the firing rate v_0 in the running state:

$$D_{\text{eff}} = \frac{v_0^2 r_+ r_-}{(r_+ + r_-)^3} \quad F = \frac{2D_{\text{eff}}}{\langle v \rangle} \quad \langle v \rangle = v_0 \frac{r_-}{r_+ + r_-}$$

After plugging the values into these formula, one gets the following results:

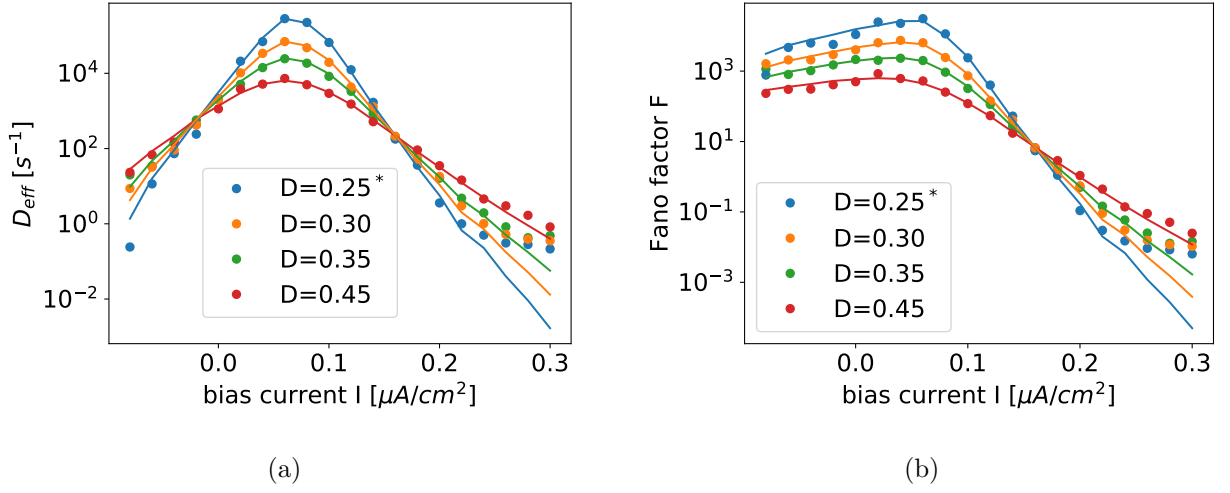


Figure 34: Point-for-point comparison of measured D_{eff} (a) and F (b) with the two-state theory based on the transition rates. The curves for $D = 0.25$ were predicted from the transition rates for the other noise intensities.

The two-state theory is able to almost exactly describe - and, in the case of $D = 0.25$, predict - the behavior of both quantities up to a bias current of $0.2 \mu A/cm^2$. After this point, the measured curves seem to saturate and do not go below a certain value whereas the two-state theory assumes exponential behavior. Thus, the theory predicts a steeper decrease of D_{eff} and F , respectively. The consistency between measurements and two-state theory now allows to make predictions for lower noise intensities.

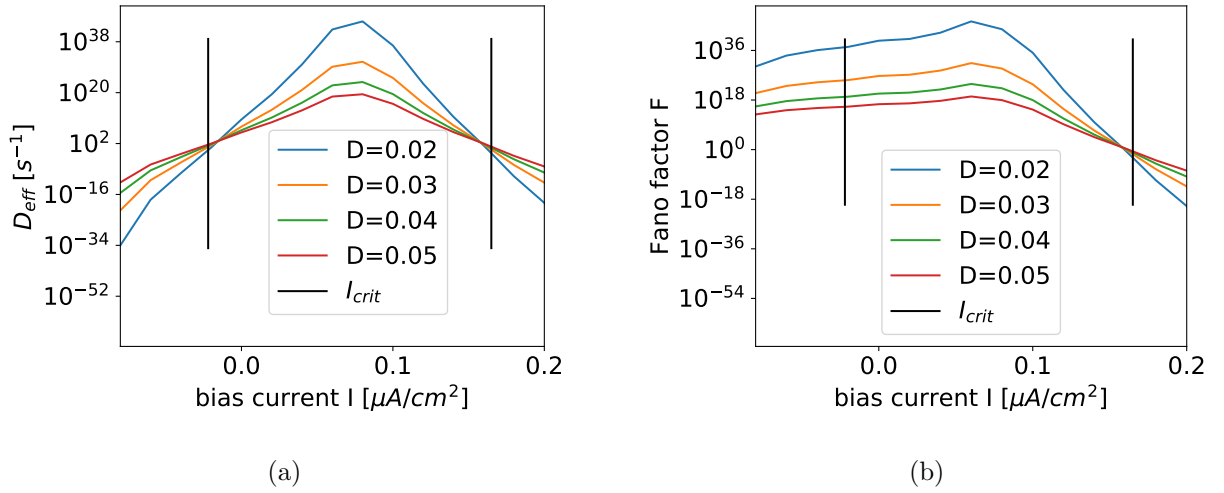


Figure 35: Point-for-point prediction of effective diffusion coefficient (35(a)) and Fano factor (35(b)) with the two-state theory

At lower noise intensities, the qualitative behavior of the measured quantities does not change much. All curves of D_{eff} intersect at two points and thereby define the region where exponential growth occurs. As before, the curves go to zero outside of this region. Here it is important to note that the curves intersect slightly earlier with respect to the maximum. This implies that the limit of $D \rightarrow 0$ has not yet been reached numerically and requires a reduction in D of about an order of magnitude

compared to the conducted simulations. However, even further decreases in D do not yield a different intersection point.

Similar to the simulations, the fano factor only has one intersection point at the right border of giant diffusion, and even though it gets maximal at the same point where D_{eff} reaches its highest value, the curves again do not seem to have a second intersection point.

4.2 $I_{Na,p} + I_K$ model with Andronov-Hopf bifurcation

4.2.1 Distribution of the state lifetimes

Again, we have to take a short look at the statistics of spiking and resting intervals first to make sure that our approach is justified. The spiking and resting intervals are clearly exponentially distributed again, so the process of changing the state is completely stochastic.

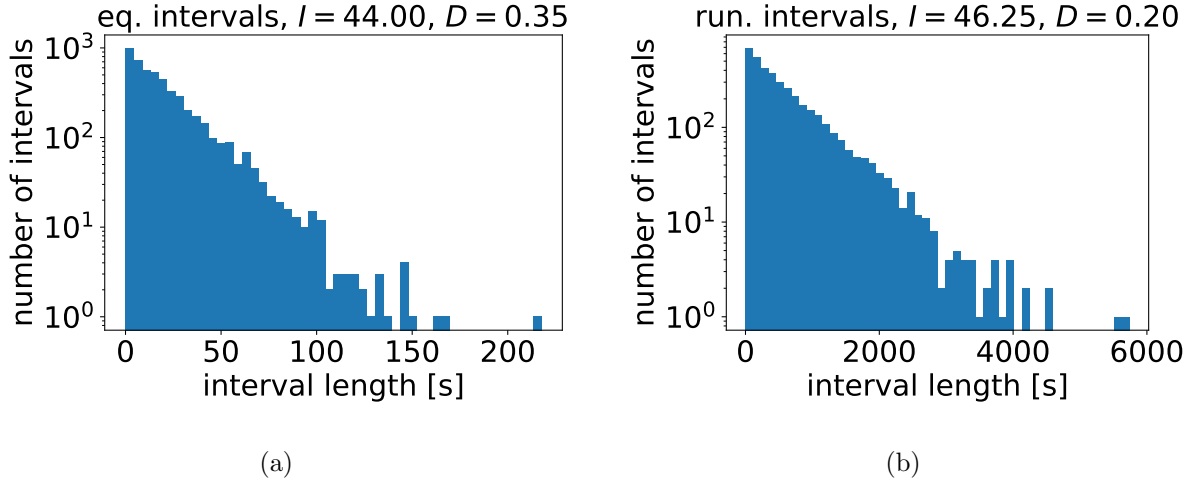


Figure 36: Distribution of equilibrium time intervals (left) and running time intervals at high switching rates

4.2.2 Transition rates at different noise intensities

It comes as no surprise that the transition rates are monotonous again.

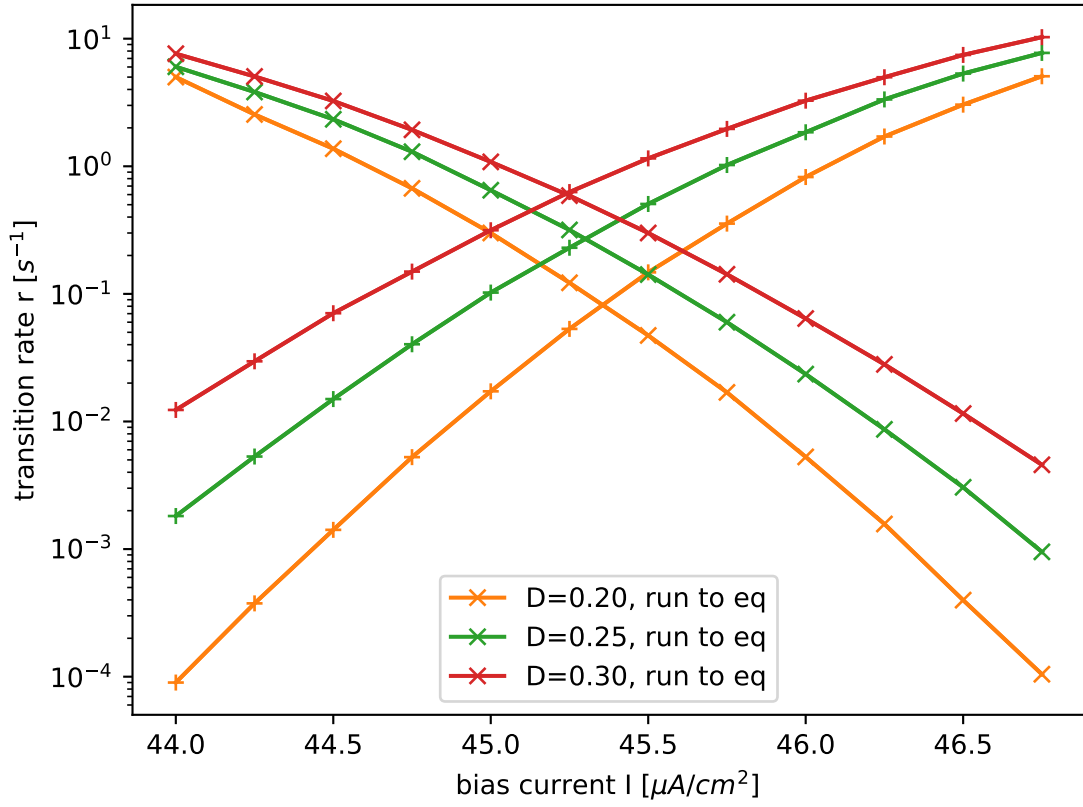


Figure 37: Transition rates between the states for a couple different noise intensities

4.2.3 Arrhenius Plots and effective potential barriers

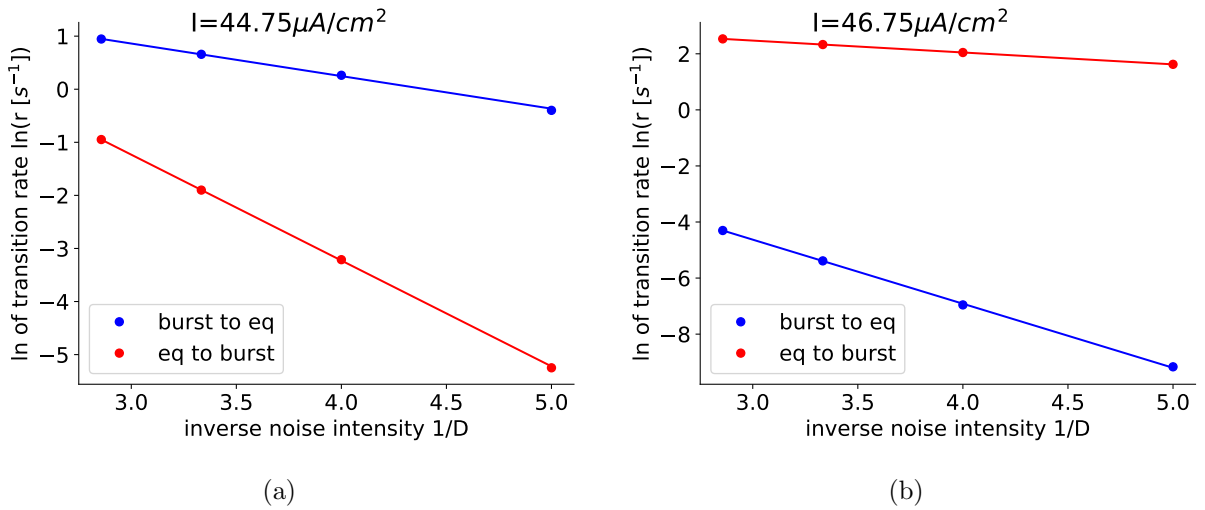
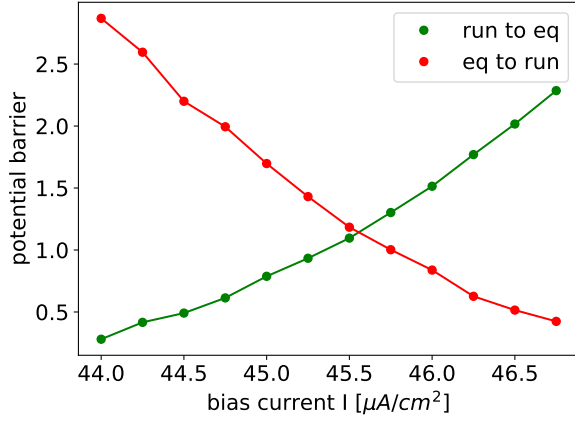
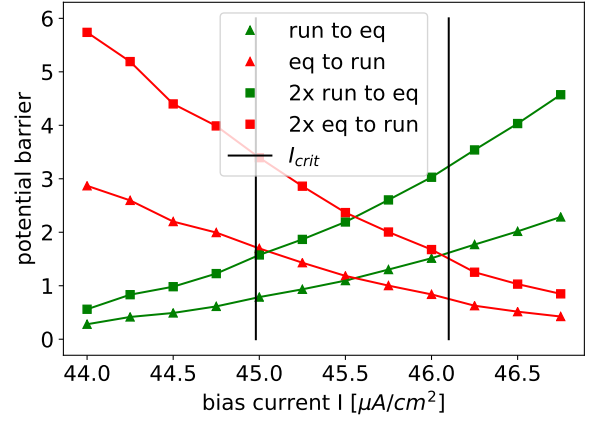


Figure 38: logarithm of the transition rates in the middle of the area with giant diffusion (a) and outside of it (b). The respective potential barriers arise from the slope of the lines.

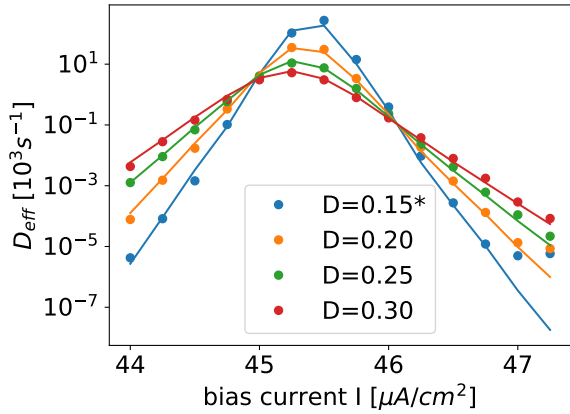


(a)

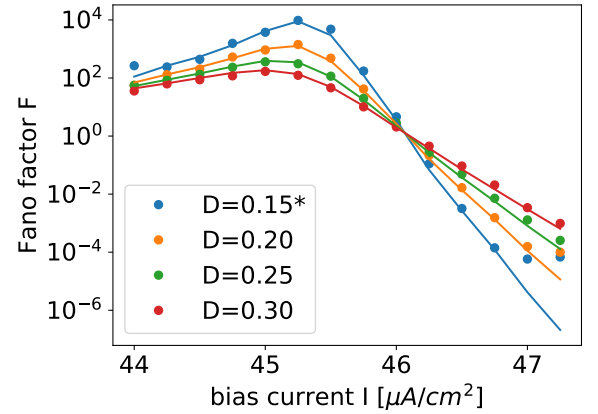


(b)

Figure 39: Effective potential barriers for both transitions. As the running state is favored at high bias currents, ΔU_+ increases, while the other one drops. The points where $\Delta U_i = 2\Delta U_j$ correspond to the numerically computed intersection points from figure 20 with only slight deviations.



(a)



(b)

Figure 40: Point-for-point comparison of measured D_{eff} (a) and F (b) with the two-state theory based on the transition rates. The curves for $D = 0.15$ were predicted from the transition rates for the other noise intensities.

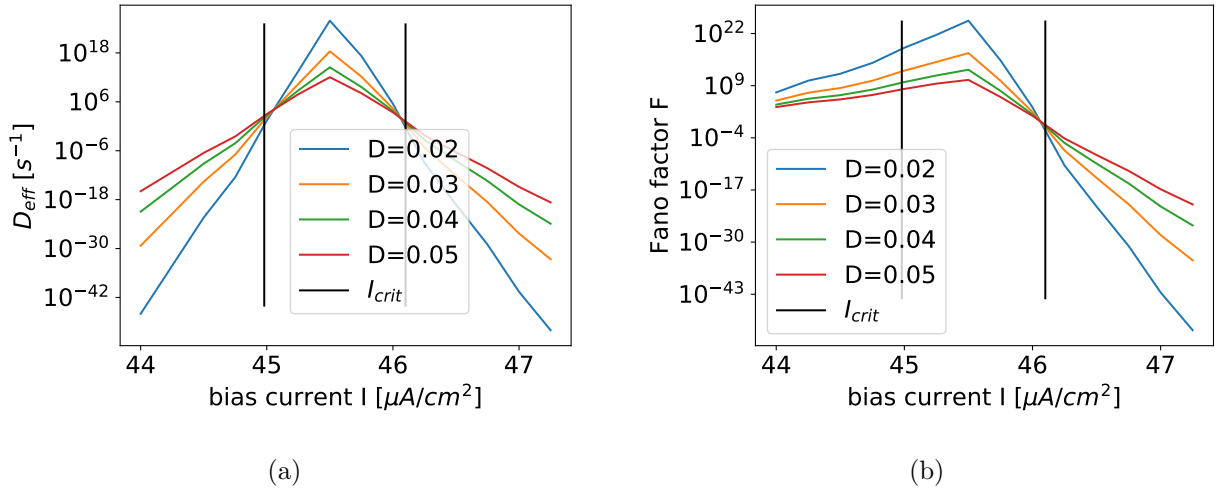


Figure 41: Point-for-point prediction of effective diffusion coefficient (41(a)) and Fano factor (41(b)) with the two-state theory

4.3 Rinzel model with saddle-node bifurcation

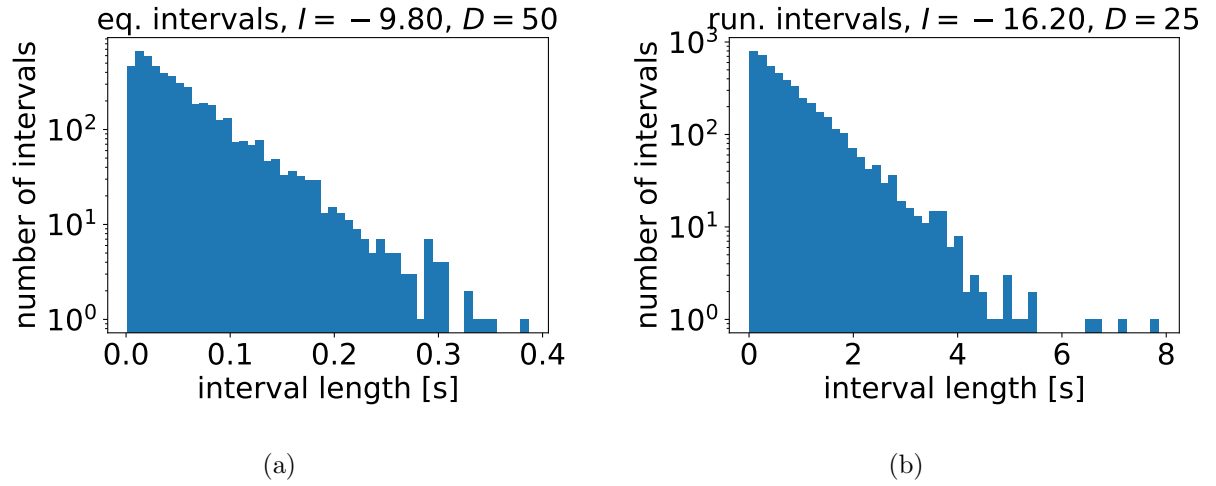


Figure 42: Distribution of equilibrium time intervals (left) and running time intervals at high switching rates

4.3.1 Transition rates at different noise intensities

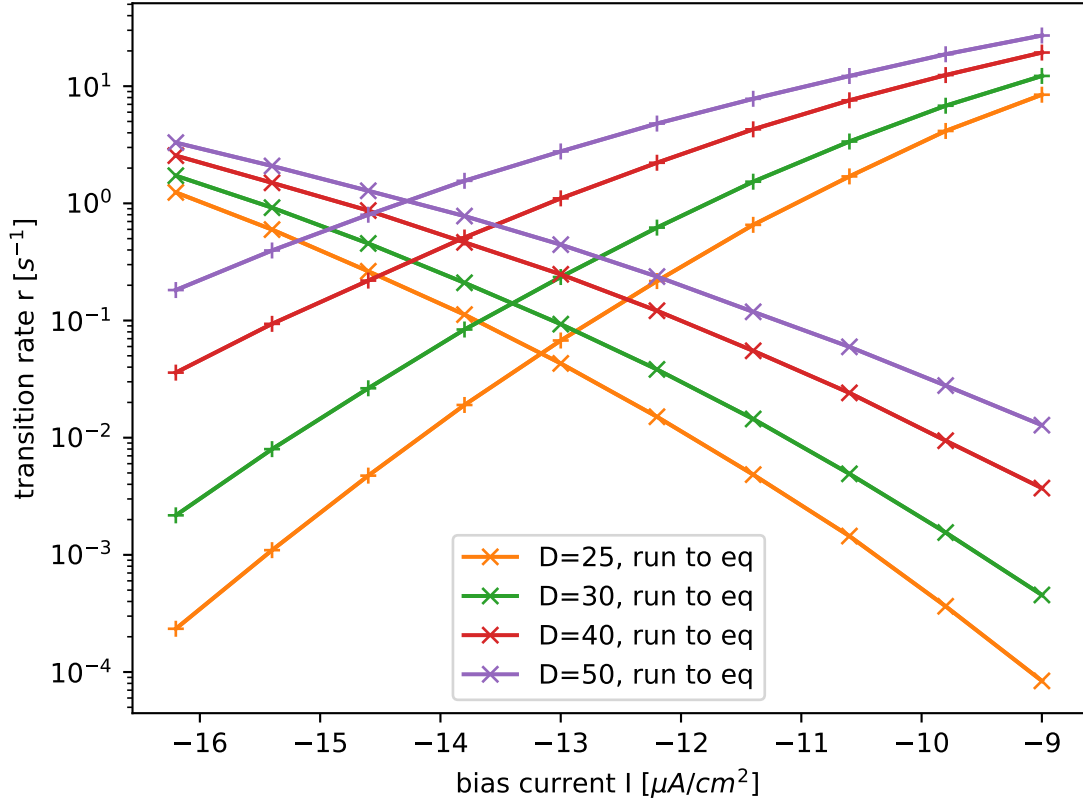


Figure 43: Transition rates between the states for a couple different noise intensities

4.3.2 Arrhenius Plots and effective potential barriers

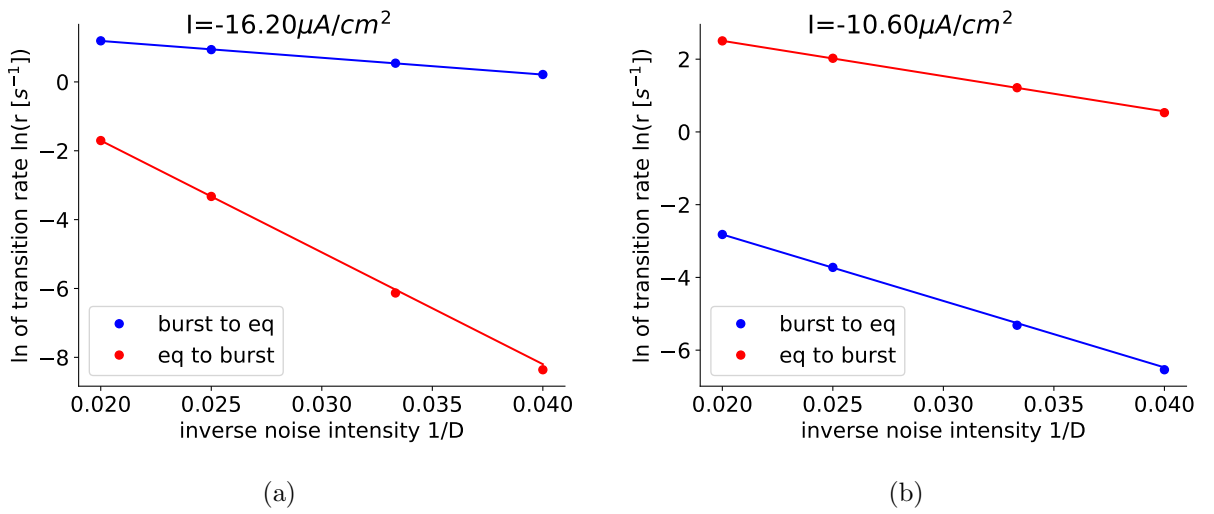
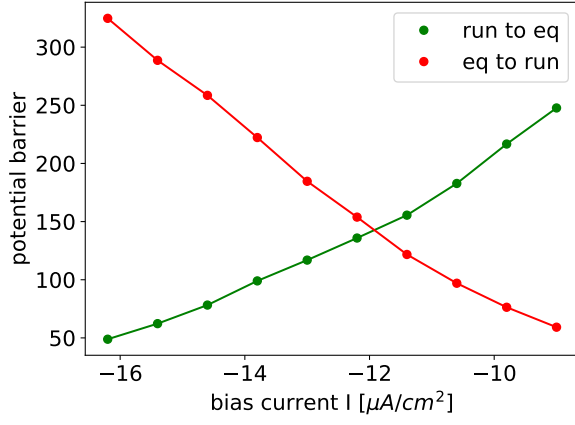
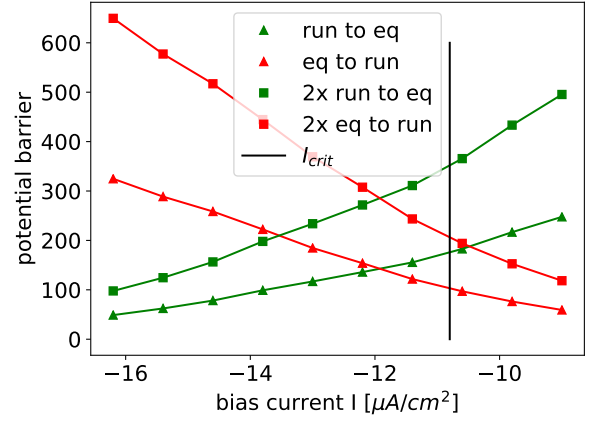


Figure 44: logarithm of the transition rates in the middle of the area with giant diffusion (a) and outside of it (b). The respective potential barriers arise from the slope of the lines.

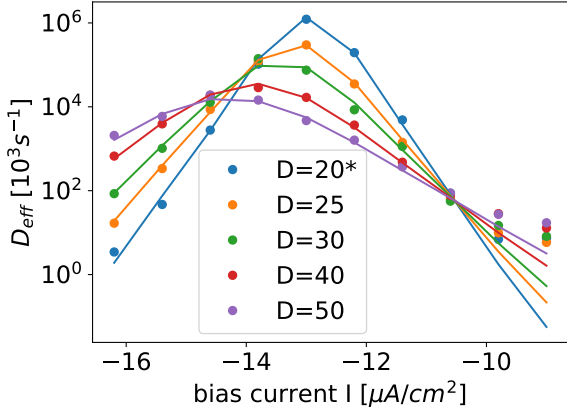


(a)

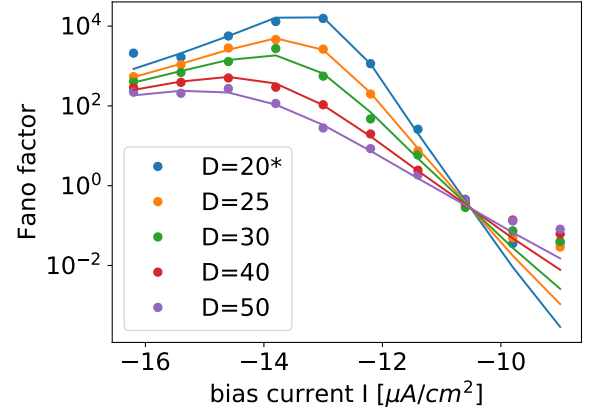


(b)

Figure 45: Effective potential barriers for both transitions. As the running state is favored at high bias currents, ΔU_+ increases, while the other one drops. The points where $\Delta U_i = 2\Delta U_j$ correspond to the numerically computed intersection points from figure 20 with only slight deviations.



(a)



(b)

Figure 46: Point-for-point comparison of measured D_{eff} (a) and F (b) with the two-state theory based on the transition rates. The curves for $D = 0.15$ were predicted from the transition rates for the other noise intensities.

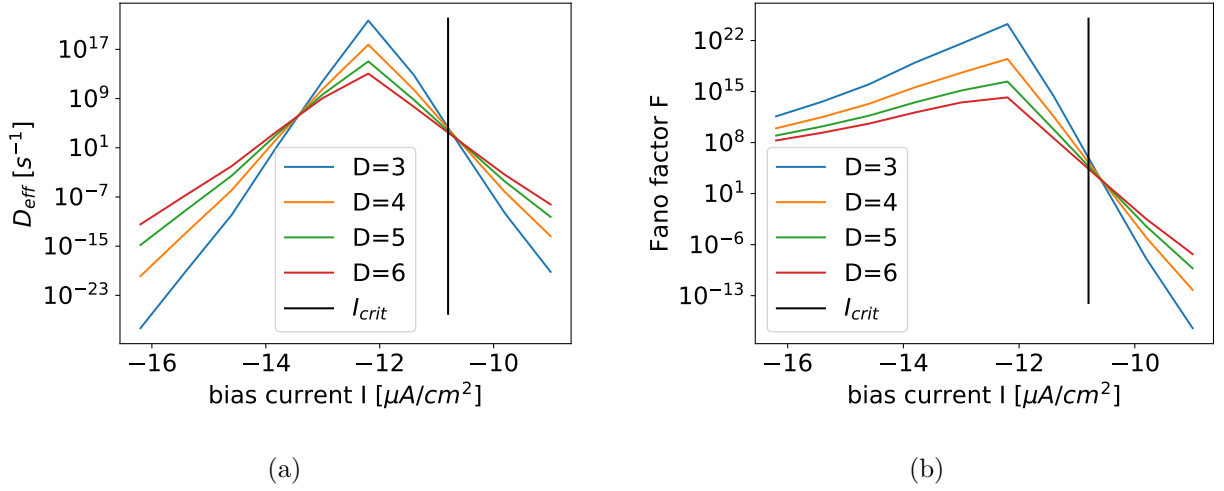


Figure 47: Point-for-point prediction of effective diffusion coefficient (47(a)) and Fano factor (47(b)) with the two-state theory

5 Consequences for Signal transmission

In the previous chapter, we clearly observed Giant Diffusion in three different neuron models. In order to understand the relevance of this finding, we need to take a look at possible applications of this phenomenon. The most obvious one in neurons is the transport of information. Therefore, we observed the behavior of the neuron models at hand under the influence of a slow periodic stimulus.

From a phenomenological point of view, there are two possible effects that a periodic signal can have on a system near the critical current. First, the effective diffusion coefficient D_{eff} is very susceptible to changes in the bias current near the critical point. Therefore, already a signal with a small amplitude may periodically shift the system from irregular firing to quite regular firing, which should be visible in the output. Secondly, one might assume that a neuron transmit information better when it is in a state of regular firing than when it fires stochastically and produces a noisy signal. Thus, the great decrease of D_{eff} outside the critical region could lead to an equal enhancement of signal transmission as the system changes from giant diffusion of the spike count to a more regular firing pattern. All in all, it is to be expected that signal transmission improves greatly when the bias current crosses its critical value.

The changes induced by a periodic stimulus can be best observed in the frequency domain. That is why we will mainly focus on the power spectrum of our signal,

$$S(f) = \lim_{T \rightarrow \infty} \frac{\langle |\tilde{x}(f)|^2 \rangle}{T} \quad (26)$$

where \tilde{x} is the fourier transform of the spike train,

$$\tilde{x}(f) = \int_0^T dt \exp(2\pi i f t) x(t) \quad (27)$$

The averaging in equation 26 is again done by cutting the spike train in segments and doing a separate Fourier transform for each segment. Hereby we had to pay respect

to the wide range of frequencies occurring in our simulations. This means that we chose a short and a longer segment length, corresponding to low-frequency and high-frequency sampling, respectively and put the spectra together at an intermediate frequency.

5.1 $I_{Na,p} + I_K$ model with saddle-node bifurcation

A lot of the characteristics of the spike train power spectrum can be well understood using the spike count statistics. For a start, there is a visible maximum at the firing rate in the spiking state, followed by a few higher harmonics. Next, the zero-frequency limit should approximately match double the effective diffusion coefficient, $S(f \rightarrow 0) \approx 2D_{eff}$, and at high frequencies, the spectrum is expected to saturate at the overall firing rate $\langle r \rangle$ [20][21]. Both of these predictions show good agreement with the spectra shown in figure 5.1. Lastly, one should mention that the membrane voltage was influenced by a periodic current, resulting in a small delta-peak at the signal frequency. The signal-to-noise ration SNR can now be calculated from the height of the delta peak and the background amplitude, which is simply the average spectral power in the vicinity of the signal peak.

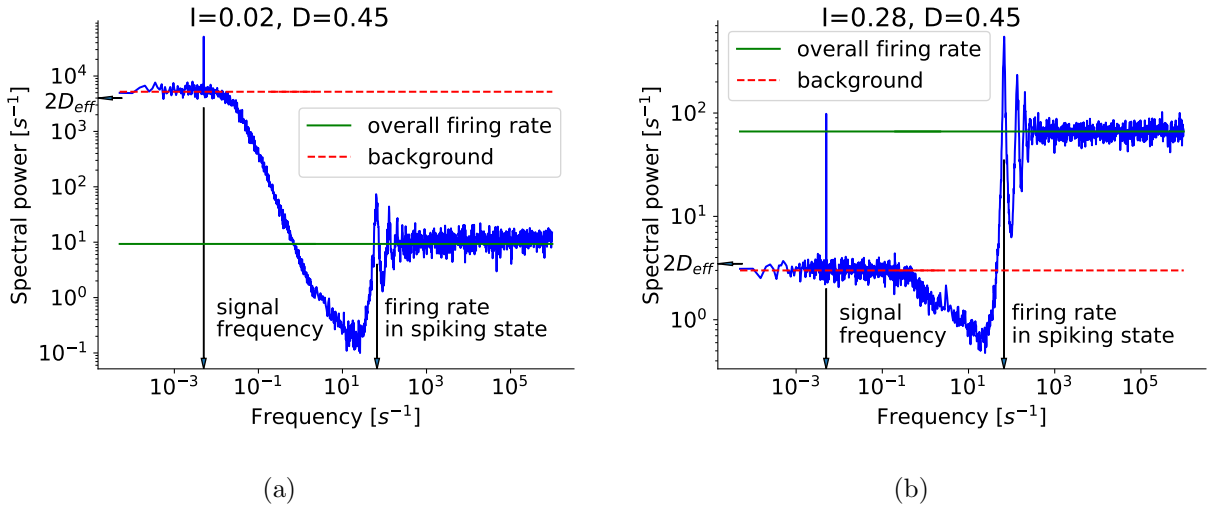


Figure 48: Spike train power spectra for the $I_{Na,p} + I_K$ model with saddle-node bifurcation. Peaks at signal and spiking frequency as well the low- and high-frequency limits agree with the theory.

The theory presented in section 2.4.2 required a weak and slow signal to find an estimate for the SNR. "Weak" in this case simply implies that the signal amplitude is small compared to the range of bias currents. Therefore, the perturbed system just slightly oscillates around the unperturbed configuration, instead of completely changing its behavior. What the keyword "slow" means, can be best seen in the power spectrum. The background amplitude shall be approximated by the zero-frequency limit. This is only valid if the signal peak lies on the plateau of the spectrum.

Since these criteria are fulfilled, we can now take a look at the SNR we obtain from these spectra.

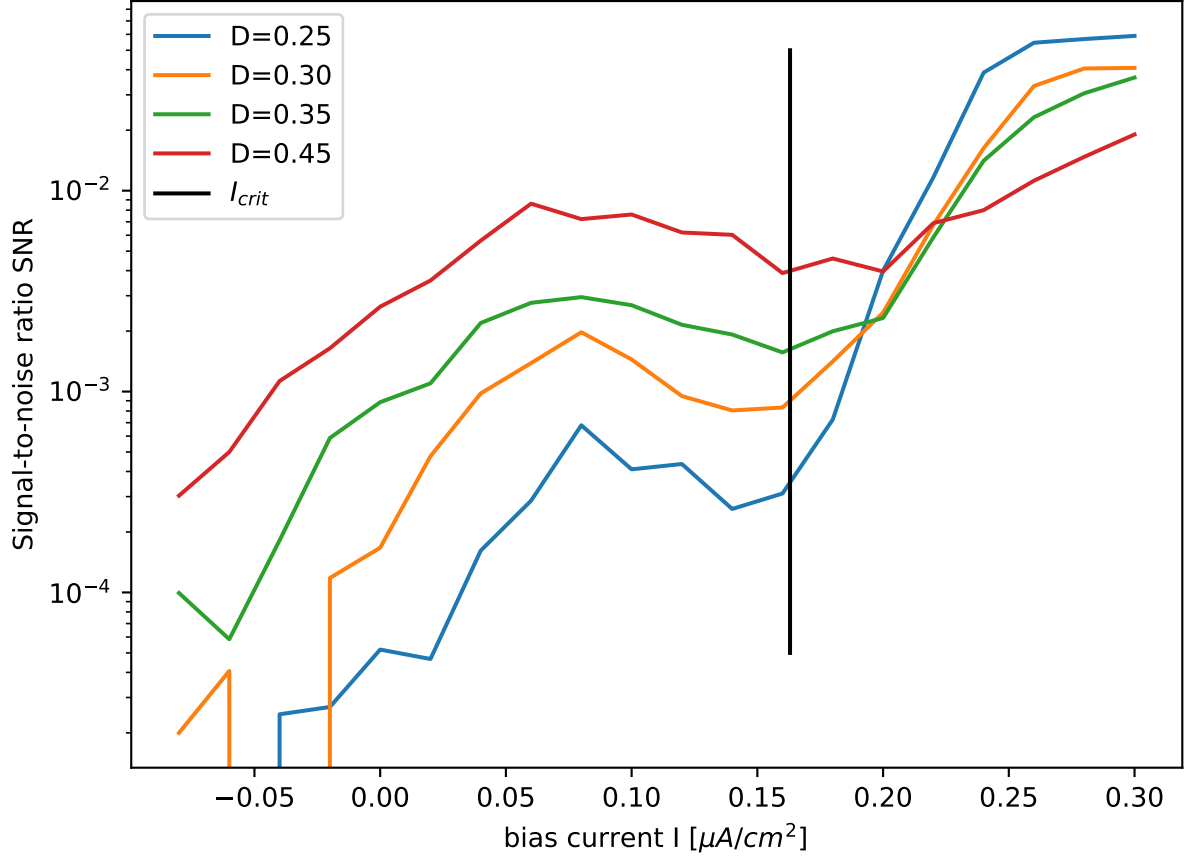


Figure 49: Signal-to-noise ratio SNR for the $I_{Na,p} + I_K$ model with saddle-node bifurcation

To begin with, the SNR greatly increases after passing the critical current by up to two orders of magnitude, thereby confirming our assumptions. However, the curves do not intersect at this point but only at a higher value. This may indicate that the noise intensities are still too low, yielding some finite-size effects. Next, all curves exhibit a maximum at almost the same bias current as D_{eff} , where the inverse proportionality of SNR and D_{eff} would imply a minimum. This can be explained by including the firing rate into our considerations. Near the maximal D_{eff} , the firing rate displays a very steep increase. Therefore, it is very susceptible to even small adjustments as induced by the signal. This effect outweighs the maximal diffusion in this case. The last aspect to discuss here is the vanishing SNR at low bias current. With regard to this observation, one has to keep in mind that neurons encode information in their spiking pattern. The neuron therefore needs to produce spikes to transport information. However, the spike count goes to zero at low bias currents, making signal transmission impossible and leading to a vanishing SNR. Fortunately, there is also a way to describe the SNR with the two-state theory, potentially leading to a deeper insight into our findings.

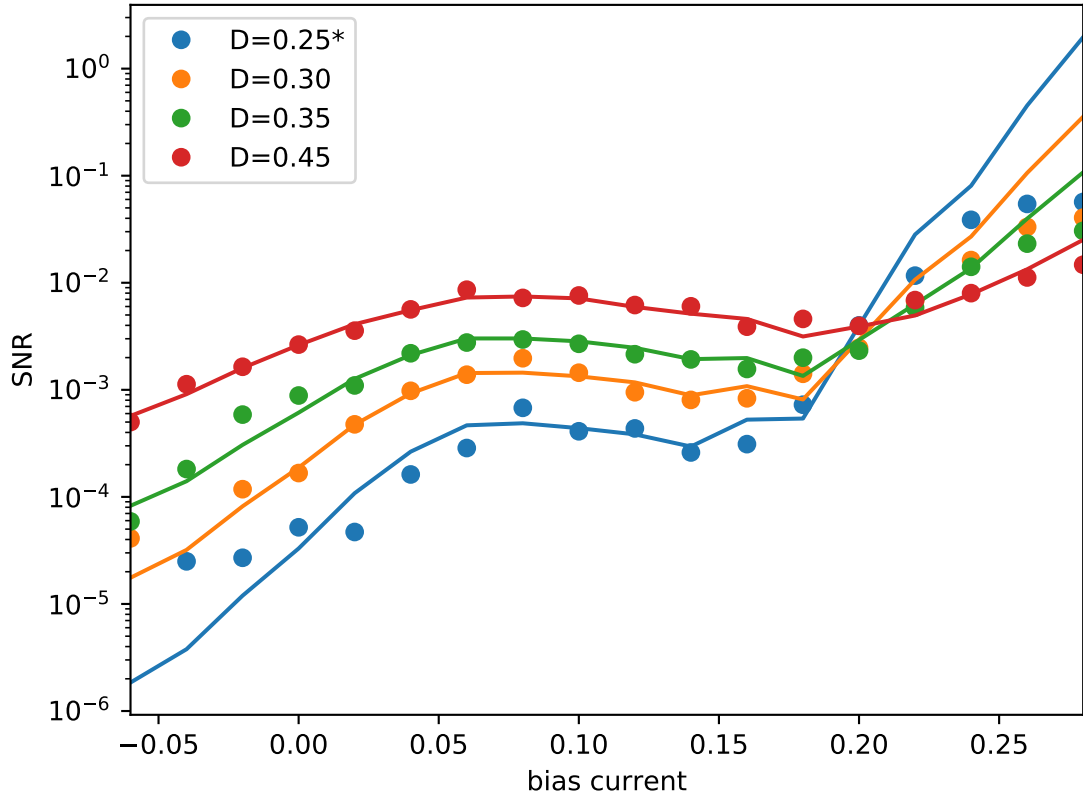


Figure 50: Comparison of Two-State theory with measured SNR for the $I_{Na,p} + I_K$ model with saddle-node bifurcation. The curve for $D = 0.25$ is a complete prediction using the transition rates of the other noise intensities.

The two-state theory is able to describe the curvature of the SNR up to a value of about $I = 0.2$, even at low noise intensities. After that, the theory overestimates the SNR. This directly corresponds to the underestimation of D_{eff} in the previous chapter, as we now have an anti-proportionality to D_{eff} . Because of the good agreement with the other data points and prediction of $D = 0.25$, we can now try to predict the SNR at lower noise intensities with the Two-State Theory.

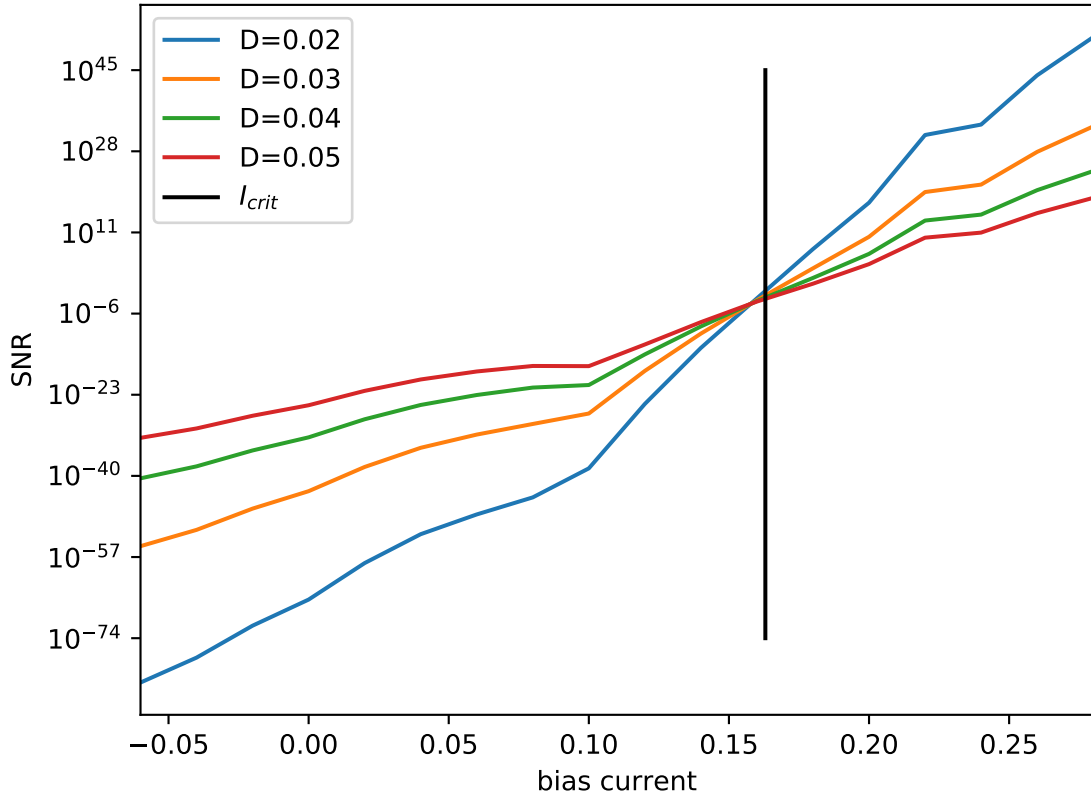


Figure 51: Prediction of SNR at low noise using the Two-State Theory for the $I_{Na,p} + I_K$ model with saddle-node bifurcation.

At low noise, the Two-State model predicts a monotone increase of the SNR. Furthermore, all curves now intersect at the same point where the predicted curves of D_{eff} cross each other, so we have reached consistency in this regard. The fact that the curves seem to increase endlessly has to be considered carefully. After the system undergoes the saddle-node bifurcation, only the spiking state exists. At this point, the signal can not induce transitions between the two firing regimes anymore, so one should expect that the SNR saturates eventually.

5.2 $I_{Na,p} + I_K$ model with Andronov-Hopf bifurcation

Seeing that signal transmission could be enhanced by multiple magnitudes near the critical current for one model, it would be interesting to find out whether this holds true for other models and which factors may have an impact there. The power spectra look similar to the first model: the curves start approximately at $2D_{eff}$, then decrease to a minimum shortly before the peak at the (maximal) firing rate appears, and finally converge to the overall firing rate. Furthermore, it is noticeable that the spectra display more maxima at higher frequencies than before, which may be due to the more irregular stable limit cycle, as mentioned in section 2.2.1.

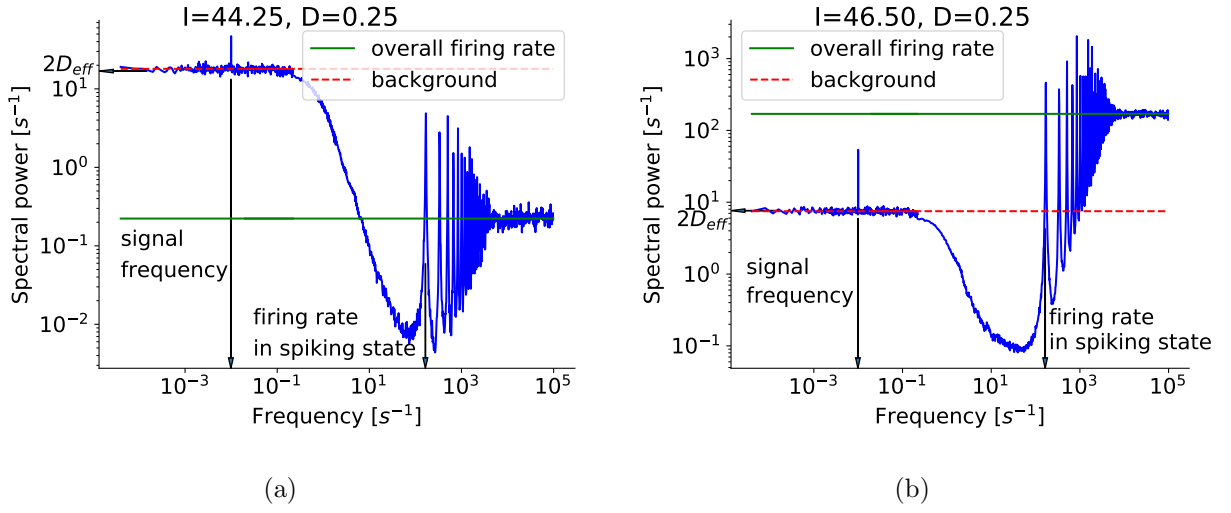


Figure 52: Spike train power spectra for the $I_{Na,p} + I_K$ model with Andronov-Hopf bifurcation. Peaks at signal and spiking frequency as well the low- and high-frequency limits agree with the theory.

Finally, one should again note that the criterion of small signal frequencies is well fulfilled in this case, which leads us to the SNR over the whole range of bias currents in figure 53.

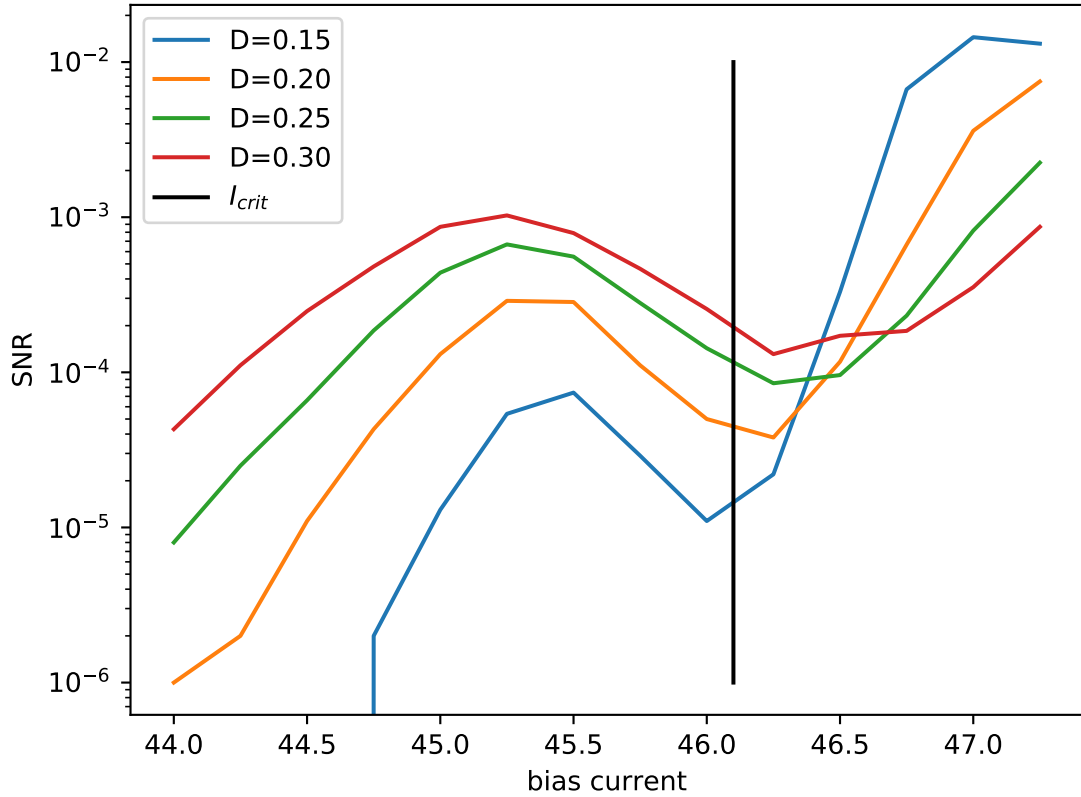


Figure 53: Signal-to-noise ratio SNR for the $I_{Na,p} + I_K$ model with Andronov-Hopf bifurcation

The N-shaped curvature is more pronounced than before, but apart from that, we have a similar picture. After the critical current, the SNR rises by up to three orders of magnitude and the intersection point is located left of I_{crit} . Next, we will take a look at the Two-state theory to confirm the reliability of our measurements and predict the outcome at lower noise intensities D .

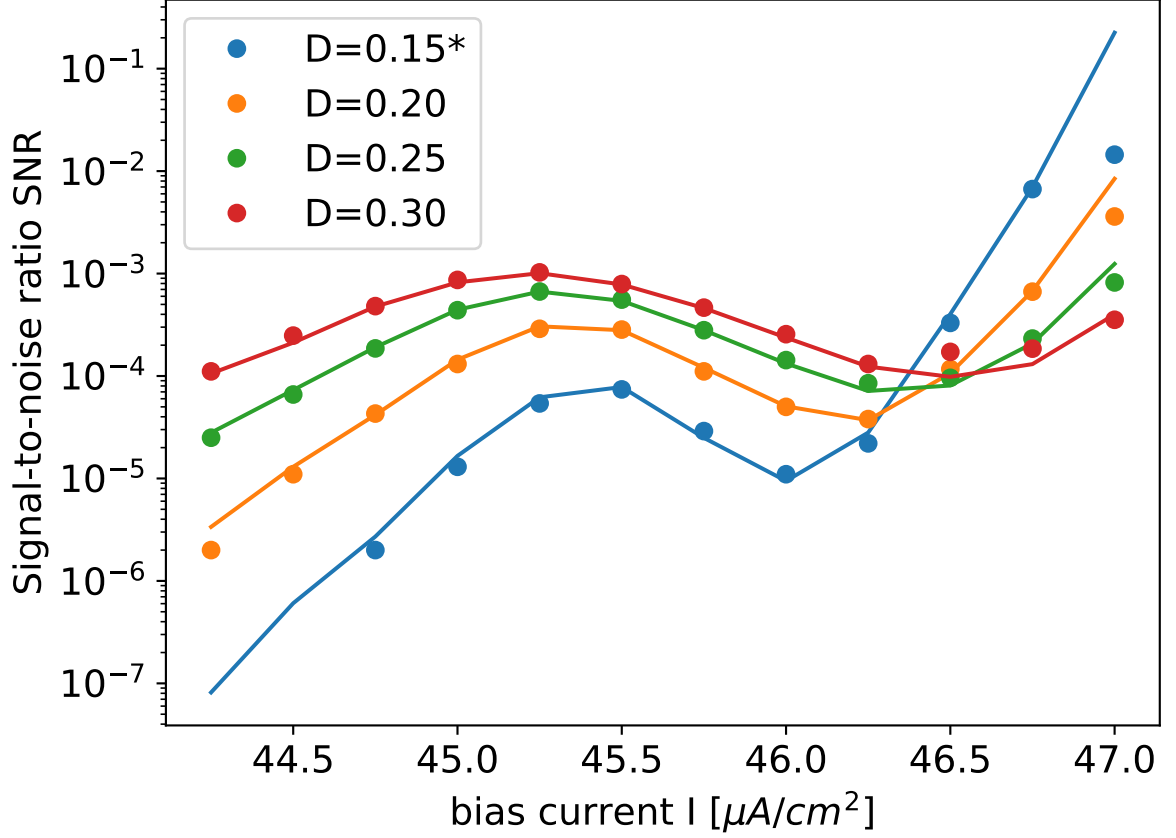


Figure 54: Comparison of Two-State Theory with measured SNR for the $I_{Na,p} + I_K$ model with Andronov-Hopf bifurcation. The curve for $D = 0.15$ is a complete prediction using the transition rates of the other noise intensities.

Almost over the whole range of bias currents, the Two-State Theory shows excellent agreement with our measurements. Only at the highest current, the theory gives slightly overestimates the SNR. This now allows to go to lower noise intensities.

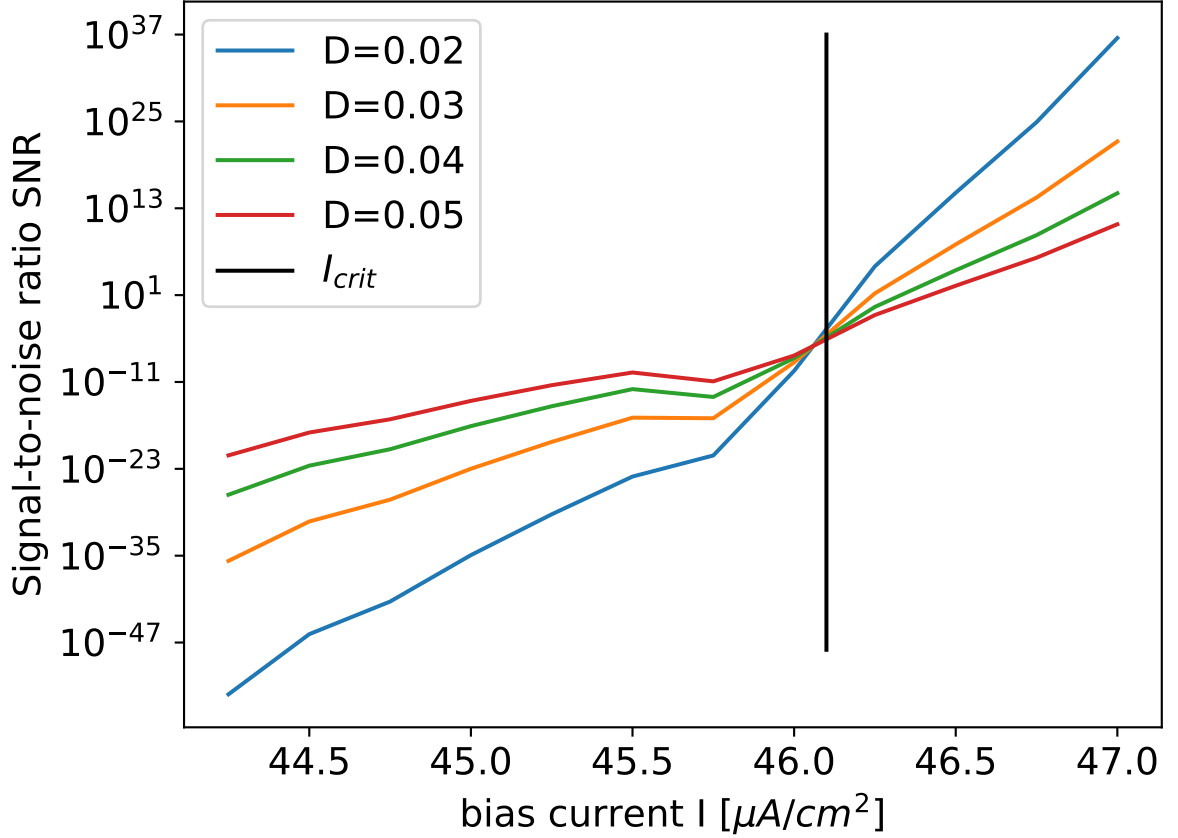


Figure 55: Prediction of SNR at low noise using the Two-State Theory for the $I_{Na,p} + I_K$ model with Andronov-Hopf bifurcation.

Surprisingly, the N-shape remains until $D = 0.03$, before the curves finally become monotone. We see that the intersection point is now slightly left of the critical current, similarly to D_{eff} at low noise. Even though the noise intensities has decreased by just an order of magnitude, the SNR now went up by more than 40 orders of magnitude after the critical current, underlining the potential that lies within these systems.

5.3 Rinzel model with saddle-node bifurcation

Surprisingly and despite its much more complex phase space picture, the spectrum for the Rinzel model looks familiar. The high-and low-frequency limits correspond to their theoretical predictions and there are peaks at signal and spiking frequency, including some higher harmonics for the latter.

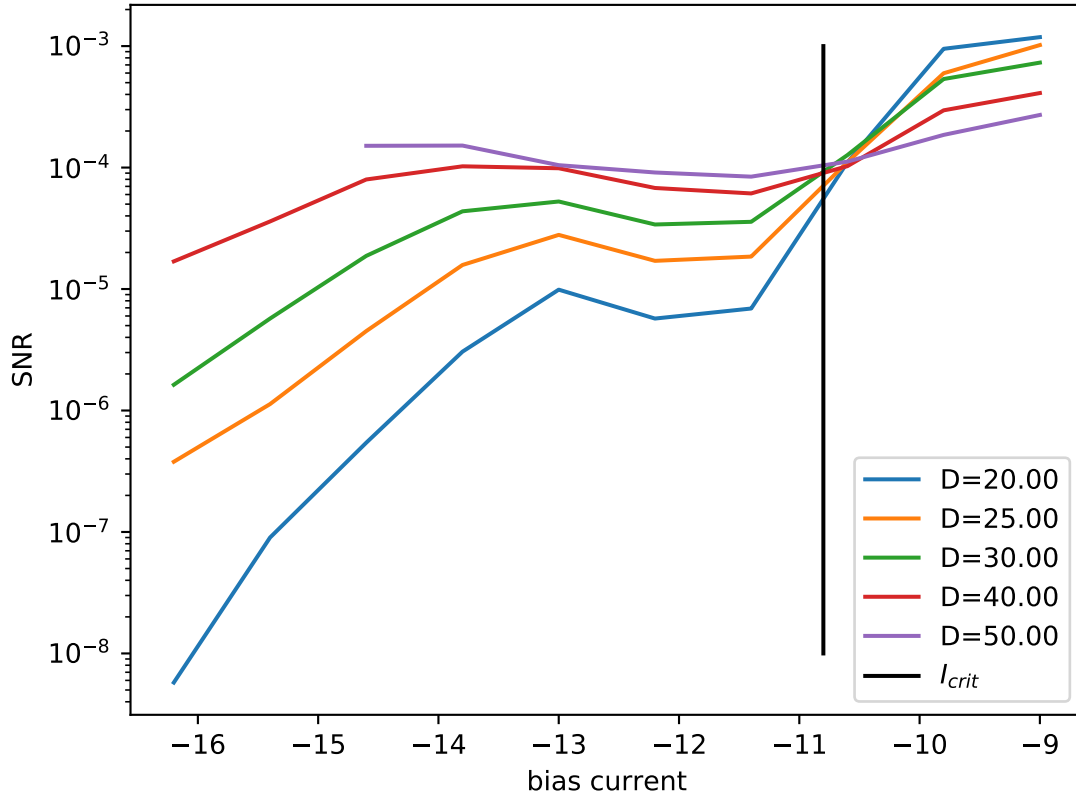


Figure 56: Signal-to-noise ratio SNR for the Rinzel model with Saddle-node bifurcation

Also the N-shape of the SNR resembles the previous models, except that it already increases before the critical current. Here, we see a maximum rise of a bit more than two orders of magnitude.

6 Conclusions

References

- [1] F. Azevedo et al., “Equal Numbers of Neuronal and Nonneuronal Cells Make the Human Brain an Isometrically Scaled-Up Primate Brain,” *The Journal of Comparative Neurology* 513, 2009.
- [2] Eugene M. Izhikevich, *Dynamical Systems in Neuroscience*. The MIT Press, 2007.
- [3] Gennady S. Cymbalyuk, “Dynamics of neuronal bursting,” *J Biol Phys* 37, 2011.
- [4] J. Jalife and C. Antzelevitch, “Phase resetting and annihilation of pacemaker activity in cardiac tissue,” *Science Vol. 206, Issue 4419*, 1979.
- [5] G. V. Di Prisco et al., “Role of Sensory-Evoked NMDA Plateau Potentials in the Initiation of Locomotion,” *Science Vol. 278, Issue 5340*, 1997.

- [6] Y. Loewenstein et al., “Bistability of cerebellar Purkinje cells modulated by sensory stimulation,” *Nature Neuroscience* 8, 2005.
- [7] Chie-Fang Hsiao et al., “Ionic Basis for Serotonin-Induced Bistable Membrane Properties in Guinea Pig Trigeminal Motoneurons,” *J. Neurophysiol.* 79, 1998.
- [8] Jorn Hounsgaard and Ole Kiehn, “Serotonin-induced bistability of turtle motoneurons caused by a nifedipine-sensitive calcium plateau potential,” *J. Physiol.* 414, 1989.
- [9] E. Marder et al., “Memory from the dynamics of intrinsic membrane currents,” *PNAS* 93, 1996.
- [10] A. V. Egorov et al., “Graded persistent activity in entorhinal cortex neurons,” *Nature* 420, 2002.
- [11] Pablo Fuentealba et al., “Membrane Bistability in Thalamic Reticular Neurons During Spindle Oscillations,” *J. Neurophysiol.* 93, 2005.
- [12] B. Lindner and I. M. Sokolov, “Giant diffusion of underdamped particles in a biased periodic potential,” *PRL* 93, 2016.
- [13] B. Lindner and E. M. Nicola, “Critical Asymmetry for Giant Diffusion of Active Brownian Particles,” *PRL* 101, 2008.
- [14] L. Gamaitoni et al., “Stochastic resonance,” *Rev. Mod. Phys.* 70, 1998.
- [15] L. V. Moran and L. E. Hong, “High vs Low Frequency Neural Oscillations in Schizophrenia,” *Schizophr Bull* 37, 2011.
- [16] J. R. Hughes, “Gamma, fast, and ultrafast waves of the brain: Their relationships with epilepsy and behavior,” *Epilepsy & Behavior* 13, 2008.
- [17] K. Nakajima et al., “Dynamic characteristics of a simple bursting neuron model,” *NOLTA Vol.* 3, 2012.
- [18] X. Zhao et al., “Low dimensional model of bursting neurons,” *J Comput Neurosci* 36, 2014.
- [19] John Rinzel, “Excitation dynamics: insights from simplified membrane models,” *Federation Proc* 44, 1985.
- [20] R. F. O. Pena et al., “Self-Consistent Scheme for Spike-Train Power Spectra in Heterogeneous Sparse Networks,” *Frontiers in Comp. Neuroscience*, 2018.
- [21] S. Vellmer and B. Lindner, “Theory of spike-train power spectra for multidimensional integrate-and-fire neurons,” *Phys. Rev. Research*, 2019.

Selbständigkeitserklärung

Ich erkläre hiermit, dass ich die vorliegende Arbeit selbständig verfasst und noch nicht für andere Prüfungen eingereicht habe. Sämtliche Quellen einschließlich Internetquellen, die unverändert oder abgewandelt wiedergegeben werden, insbesondere Quellen für Texte, Grafiken, Tabellen und Bilder, sind als solche kenntlich gemacht. Mir ist bekannt, dass bei Verstößen gegen diese Grundsätze ein Verfahren wegen Täuschungsversuchs bzw. Täuschung eingeleitet wird.

Berlin,